Natural Disaster Science, Volume 8, Number 1, 1986, pp. 55–84

MECHANISM OF SLOPE FAILURE DURING HEAVY RAINFALL IN NAGASAKI JULY 1982

Tetsuya ISEDA
Professor, Faculty of Civil Engineering, Nagasaki University
and
Yoshihiko TANABASHI
Research Associate, Faculty of Civil Engineering, Nagasaki University

(Received 16 Jan., 1986 and in revised form 16 June, 1986)

ABSTRACT

On Juy 23, 1982, 299 human lives were lost in Nagasaki Prefecture due to localized heavy rainfall, nearly 90% of which were due to sediment disaster. So, it is important to clarify a mechanism of slope failure during heavy rainfall for sediment disaster prevention.

In this paper, we firstly carry out a model experiment of slope failure due to infiltration and observe a phenomenon in progressive failure of slope. Secondly, we apply a finite element analysis which is divided into two stages, i.e. a saturated-unsaturated seepage flow analysis and a stability analysis taking into account the seepage force and the reduction of strength due to the rise in the degree of saturation, to two actually failured slope in Nagasaki city. And we check their failure under the conditions of preceding rainfall, rainfall on the day of failure, topography, geology and so on.

Finally, we have clarified a mechanism of slope failure during heavy rainfall and shown that slope failure can be predicted if a rise in the groundwater table can be detected.

1. INTRODUCTION

On July 23, 1982, 299 human lives were lost in Nagasaki Prefecture due to localized heavy rainfall during the latter part of Japanese rainy season, nearly 90% of which were due to such slope failures as landslides, rockfalls, debris flow, etc..

Geomorphologically distinctive features [1] of the slope failures in the total 143 failures are

(a) *Slope Height*:

70% of the failures occurred on slopes whose vertical heights were less than 30 m (the national average is 60%). This means that failures took place on slopes of comparatively small height.

(b) *Slope Angle*:

45% of the failures occurred at slope angle of 30°~39°, and 30% at angle of 20°~29°. Failures in Nagasaki Prefecture were more frequent on gentle slopes than the national average, greatest frequency at 40°~49° (36.2%), would indicate.

(c) *Slope Shape*:

(i) *Cross section type failure*

Past failures have been said to occur when large amounts of rain fell on concave contour slope. But in this case, the major portion of failures took place on planer slopes.

(ii) *Longitudinal section type failure*

These failures occurred on rectilinear slopes. On the basis of the given geomorphological features the normal stability calculation for a saturated slope of infinite length with a top soil layer of 2-m thick gives 2.0 as the safety factor [2].

KEY WORDS: seepage, seepage force, slope disaster, finite element analysis
Note: Discussion open until 1 Sept. 1987

We therefore modeled our experiments on conditions of the stability of slopes under the seepage force, assuming that seepage participated in slope failure. By applying finite element analysis of non-stationary saturated-unsaturated seepage flow to our model experiment and by taking the body forces including the seepage force and the gravity force into account for each element, we could determine the stability of the slope at a given time. Two actually failed slopes were chosen in Okuyama area and in Hokuei-cho, Nagasaki city and their failures checked under the conditions of preceding rainfall, rainfall on the day of failure, topography, geology, soil properties, etc. at each location.

2. MODEL EXPERIMENT

This experiment was done to determine whether a slope, whose safety factor was 2.1 calculated by an infinite slope method, would collapse or not by taking the seepage flow into account.

The design of the model experiment shown in Fig. 1 was used. The water table in the soil layer was changed from X–X to Y–Y, and the height or position of Y–Y at which the layer of soil would fail was sought.

2.1. *Soil Specimen and Apparatus*

The soil specimen was taken from the Okuyama area. It belongs to MH in the Japanese unified soil classification system. The soil was placed in the test box (shown in Fig. 1) and was tamped down to the density of the ground at the failure-field site, thus forming the model slope. A comparison of soil properties the failure-field site and for the experimental slope is shown in Table 1. Although the values did not coincide for water content, compaction, etc., we decided to base our calculations by using that for the experimental slope.

To simulate the highly porous, weathered layer which was confirmed by the boring log in the Okuyama area between the collapsed soil layer and the base rock, we laid a sheet of corrugated card board with numerous small perforations at the bottom of the model slope. But, because water in the tank (T) was supplied through the point (V), perforations on the card board surface around the point (V) were omitted to avoid possible boiling failure of the soil layer just

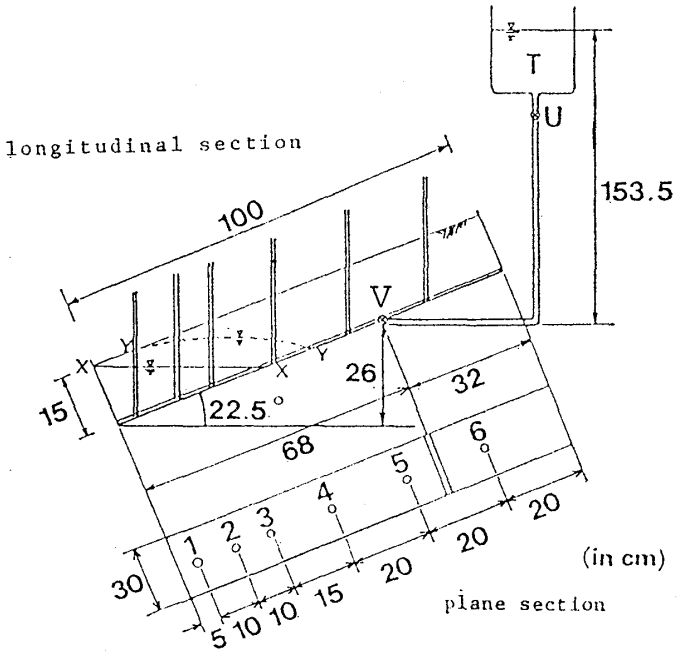

Fig. 1 Design of the apparatus for the model experiment.

Table 1 Soil properties in the model slope and the site.

Parameter	Symbol	Model	The site
Void ratio	e	2.076	1.387
Natural water content (%)	W_n	53.0	38.6
Degree of saturation (%)	S_r	69.7	76.0
Specific gravity of soil particles	G_s	2.73	2.73
Wet density (g/cm³)	ρ_t	1.36	1.59
Dry density (g/cm³)	ρ_d	0.888	1.144

above the point (V). But, if the tank has excessive height, boiling in this area is inevitable; therefore, the height of the tank was determined by trial and error.

Manometers were placed so as to rise vertically from the bottom of the soil layer and used to confirm the pore water pressure generated below the ground surface. The positions of the manometers were arranged with close pitches toward the lower end of the slope in anticipation of the position of failure (see Fig. 1).

2.2. *Experiments and Results*

Prior to the experiment, a small quantity of water was supplied through the point (V) to make the water table in the soil layer horizontal. The experiment was begun by fully opening the cock (U) and checking the water level in the tank (T) and the pore water pressure indicated by the manometers. The water level in the tank is given in Fig. 2, the supply discharge is given in Fig. 3 and the manometer readings a intervals of 4 min in Fig. 4.

The water level in the tank was adjusted by another supply of water 20 min after the experiment had been started to keep the initial total head at the point (V) constant. Changes that occurred in the quantity of inflow (Fig. 3), influenced the fluctuation of the water level as indicated by the manometers (Fig. 4). But, the absolute value of the quantity of inflow being very large, the variations in the water level in the tank had little effect on the potential which is the output of analytical calculations.

Collapse occurred 28 min after the experiment had begun, but boiling did not occur in the model slope. Manometer readings (Fig. 4) and the conditions until collapse showed that the gushing out of water at the lower end of the slope, observed at the beginning of the experiment, increased 18 min after, and at 21 min, conspicuous cracks were generated on the surface of the

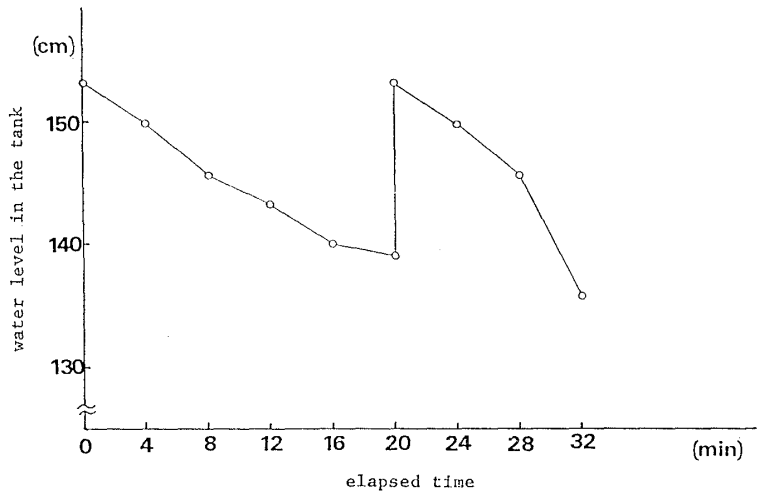

Fig. 2 Variation in the water level in the tank with time.

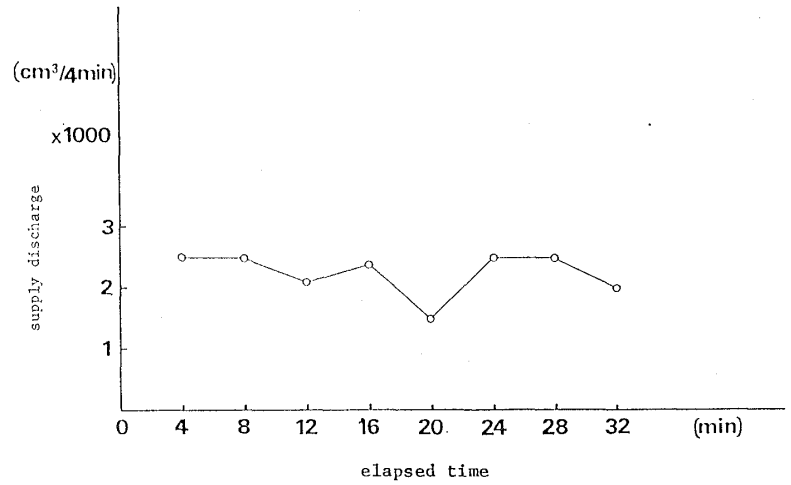

Fig. 3 Variation in the supply discharge with time.

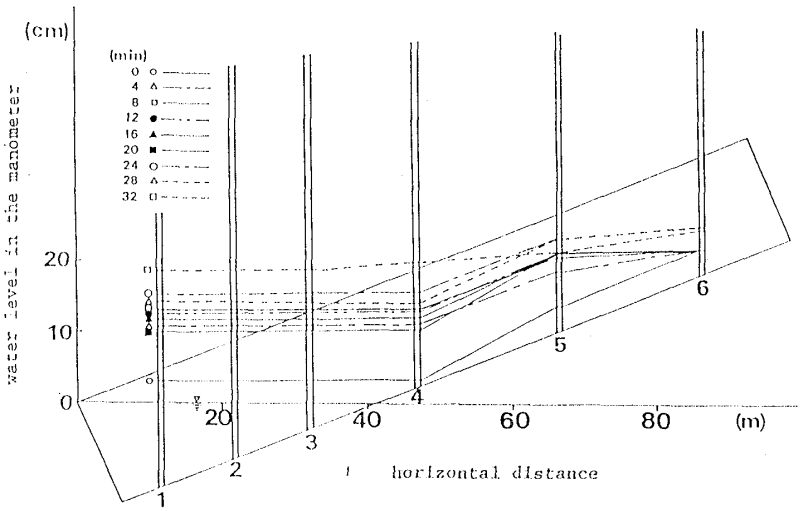

Fig. 4 Variation in the water level in manometers with time.

slope in a direction normal to the slope's inclination. At 22 min the soil layer at the lower end began to bulge, and at 23 min a small scale failure took place at the lower end of the slope. At 24 min, the failure was propagating and from 26 to 28 min, a very large scale failure occurred. The model slope was destroyed by the large quantity of a mixture of spring water and collapsed soil flowing down.

3. METHOD OF ANALYSIS

The analysis was divided into two stages; a saturated-unsaturated seepage flow analysis (hereinafter called FEM-A), and a stability analysis (hereinafter called FEM-B) that took into account the seepage force and the reduction of strength due to the rise in the degree of saturation.

3.1. *FEM-A*

In this stage of analysis, we used the method of Akai, Ohnishi and Nishigaki [4], in which the fundamental equation that determines seepage in the saturated-unsaturated range is represented by Eq. (1).

$$\text{div}\, K(\theta)\cdot\nabla(\varphi+z) = (c(\theta)+\alpha\cdot S_s)\frac{\partial\varphi}{\partial t} \tag{1}$$

in which $K(\theta)$ is the coefficient of permeability tensor of the 2nd order, φ the pressure head, θ the volumetric water content, z the potential head, $c(\theta)=\partial\theta/\partial\varphi$, the specific water capacity, S_s is the specific storage coefficient ($\alpha=0$ in the unsaturated range and $\alpha=1$ in the saturated range).

Eq. (1) is formulated with the finite element by applying the weighted residual method and with respect to time (t) the iterative procedure by finite difference method is applied. To make a numerical analysis under arbitrary conditions by applying Eq. (1), the relation between the pressure head (φ) and the volumetric water content (θ), the relation between the relative conductivity (K_r) and the coefficient of permeability under saturated condition (K_{sat}), the initial pressure head (φ_0) and the initial volumetric water content (θ_0) must be used as the input data. As output, the total head ($H=\varphi+z$), the pressure head (φ) and the volumetric water content (θ) at every nodal point are gained for any arbitrarily chosen time (t).

3.2. *FEM-B*

Using the results gained by FEM-A, we then made a stability analysis taking into account the seepage force and the reduction of strength due to the rise in the degree of saturation as follows.

(1) *Relation between the degree of saturation and shear strength*

Applying the results of Kudara [5], we could approximate the relation between the degree of saturation (S_r) and the strength constants (c', ϕ') with a hyperbola as represented by Eq. (2).

$$c'(S_r) = 1/(a\cdot S_r+b) \tag{2}$$

in which

$$a = (1/c_1'-1/c_i')/(1-S_r)$$
$$b = 1/c_1'-a$$

Of the subscripts, (i) is the initial (natural) condition and (1) is $S_r=1$, the saturated condition. Therefore, c_i' is the same under the initial condition, and c_1' is the same under the saturated condition.

Similar formula is used with respect to ϕ' (S_r), $\phi_i'=\phi_1'$ is assumed, because ϕ' changes very little with the value of the degree of saturation (S_r).

The degree of saturation of a triangular element arbitrarily chosen is calculated with Eq. (3) from the volumetric water content of each nodal point θ_i, θ_j and θ_k as the output of FEM-A.

$$\{S_r\}^e = (\theta_i+\theta_j+\theta_k)/3n \tag{3}$$

in which n is the porosity.

(2) *The seepage force working on each element*

The relation of the seepage force working on each element along the stream line and the nodal forces equivalent to it is derived from Fig. 5 as follows. The total heads H_i, H_j and H_k at the respective nodal points i, j and k of an element arbitrarily chosen are taken in the direction of the H-axis and a plane that involves the triangle (pqr) is considered. The π-plane is represented by Eq. (4).

$$\pi: A\cdot x+B\cdot y+C\cdot H = D \tag{4}$$
$$A = H_i(y_k-y_j)+H_j(y_i-y_k)+H_k(y_j-y_i)$$
$$B = H_i(x_j-x_k)+H_j(x_k-x_i)+H_k(x_i-x_j)$$
$$C = x_i(y_j-y_k)+x_j(y_k-y_i)+x_k(y_i-y_j) = 2\cdot dvol$$
$$D = H_i(x_j\,y_k-x_k\,y_j)+H_j(x_k\,y_i-x_i\,y_k)+H_k(x_i\,y_j-x_j\,y_i)$$

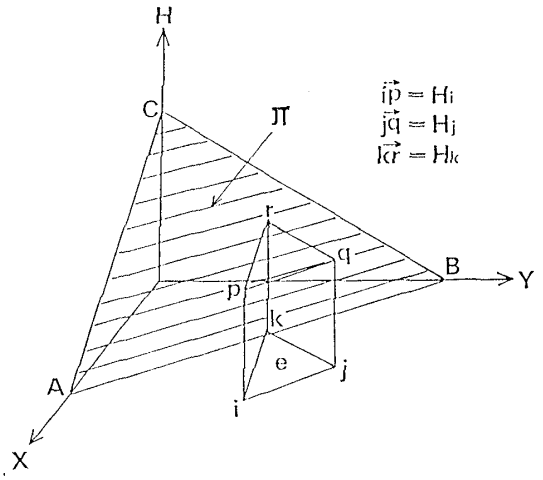

Fig. 5 Schematic diagram for deriving the seepage force.

in which x_m, y_m $(m=i, j, k)$ are the coordinates of each nodal point, $(dvol)$ is the volume of each element and $H_m(=\varphi_m+z_m)$ $(m=i, j, k)$, is the total hydraulic head of each nodal point.

And, because the hydraulic gradient along the x-direction of element (e), $\{i_x\}^e=\{\partial H/\partial x\}^e$, is the gradient of the line of intersection between the π-plane and plane $y=0$, AC along x-direction (the equation of the line of intersection AC) is represented by $Ax+CH=D$ from Eq. (4). Thus

$$\{i_x\}^e = \{\partial H/\partial x\}_{y=0} = -A/C \tag{5}$$

Similarly the hydraulic gradient along the y-direction becomes

$$\{i_y\}^e = \{\partial H/\partial y\}_{x=0} = -B/C \tag{6}$$

In addition, the seepage forces on the element (e) along the x and y-directions are represented by Eq. (7).

$$\left.\begin{aligned}\{P_X\}^e &= \gamma_w \cdot \{i_x\}^e \cdot dvol\\ \{P_Y\}^e &= \gamma_w \cdot \{i_y\}^e \cdot dvol\end{aligned}\right\} \tag{7}$$

in which γ_w is the unit weight of water.

The nodal forces f_m $(m=i, j, k)$ for the x and y-directions, which are equivalent to the seepage force, are given by Eq. (8) derived from Eqs. (5)~(7).

$$\begin{aligned} f_X &= \{P_X\}^e/3 = -\frac{\gamma_w}{6}\cdot\{H_i(y_k-y_j)+H_j(y_i-y_k)+H_k(y_j-y_i)\}\\ f_Y &= \{P_Y\}^e/3 = -\frac{\gamma_w}{6}\cdot\{H_i(x_j-x_k)+H_j(x_k-x_i)+H_k(x_i-x_j)\}\end{aligned} \tag{8}$$

(3) *Mechanical model of the soil material*

Under the initial stresses, the soil material is assumed to be an isotropic elastic body, but it is simulated after failure by replacing the elements of local failure (including the shear and tensile failures) with a cross-anisotropic material whose anisotropy has developed in the direction of the planes of slide or tensile failure and by reducing the rigidity in that direction. A failure criterion adopted here is illustrated in Fig. 6, in which the tensile zone in the Mohr-Coulomb's law is corrected with an arc that account for the failure characteristics in the tensile zone [7].

The safety factor F_s against local failure of elements defined by the following conditions can be introduced (see Fig. 6):

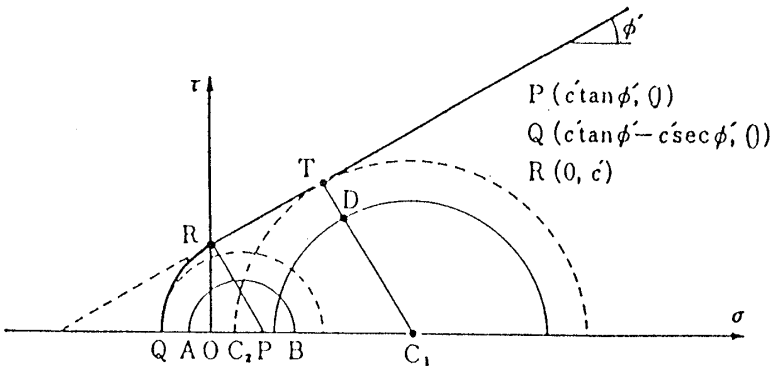

Fig. 6 Adopted failure criterion for soil.

(I) When $\sigma'_{mp} \geqq c' \tan \phi'$

$$F = \frac{C_1 T}{C_1 D} = \frac{c' \cdot \tan \phi' + \sigma'_{mp} \cdot \sin \phi'}{\tau_{\max}} \quad (F_s > 0)$$

(II) When $c' \cdot \tan \phi' > \sigma'_{mp} \geqq c'(\tan \phi' - \sec \phi')$

$$F = \frac{C_2 Q}{C_2 A} = -\frac{\sigma'_{mp} - c'(\tan \phi' - \sec \phi')}{\tau_{\max}} \quad (F_s < 0)$$

(III) When $c'(\tan \phi' - \sec \phi') > \sigma'_{mp}$

$$F = -0 \tag{9}$$

in which

$$\sigma'_{mp} = (\sigma'_1 + \sigma'_3)/2, \ \tau_{\max} = (\sigma'_1 - \sigma'_3)/2$$

σ_1 is the major effective principal stress and σ_3 the minor effective principal stress.

Shear failure occurs in elements that satisfy $0 < F_s < 1$ for the conditions of σ_{mp} in (I). Because the failure plane makes an inclination of $\pm(\pi/4 - \phi'/2)$ with the axis of the maximum compressive stress, a sign notation is selected according to the position of the element and the normal to the plane of sliding is replaced by the principal axis of an anisotropic material. Although, a significant decrease can be expected in the shear modulus in the direction of the plane of sliding after shear failure of the element, the reduction in Young's modulus in a direction normal to the failure plane could not be anticipated when elements are under compressive stress conditions. Therefore, in this case only the anisotropic shear modulus G_f is reduced to 1/1000 of its initial value $G_0 = E_0/2(1+\nu_0)$.

To addition, tensile failure occurs in elements which satisfy $-1 \leqq F_s < 0$ for the conditions of σ'_{mp} given by (II) and (III). Because, the axis of the minor principal stress is perpendicular to the failure plane, the initial isotropic material is substituted with an anisotropic one whose principal axis is normal to the failure plane. And, because a remarkable reduction in Young's modulus in the direction normal to the failure plane and a reduction in the modulus of shearing rigidity can be expected in the elements after tensile failure, the Young's Modulus (E_{2f} in the direction of the principal axis) and the shear modulus (G_f in the direction of the failure plane) are reduced to 1/1000 of their initial values. Here, the angle β measured counterclockwise between the failure plane and the x axis is given by Eq. (10).

When $\sigma'_x - \sigma'_y > 0$

$$\left.\begin{matrix}\beta_1 \\ \beta_2\end{matrix}\right\} = \arctan\left(\frac{\tau_{xy}}{\sigma'_1 - \sigma'_y}\right) \pm \left(\frac{\pi}{4} - \frac{\phi'}{2}\right)$$

When $\sigma'_x - \sigma'_y \leqq 0$

$$\left.\begin{matrix}\beta_1\\ \beta_2\end{matrix}\right\} = \arctan\left(\frac{\sigma_y'-\sigma_3'}{\tau_{xy}}\right)\pm\left(\frac{\pi}{4}-\frac{\phi'}{2}\right) \tag{10}$$

The initial isotropic stress-strain matrix $\boldsymbol{D}_{\text{iso}}$ is given by Eq. (11) and the cross anisotropic stress-strain matrix $\boldsymbol{D}_{\text{an}}$ after local failure is given by Eqs. (12) and (13).

$$\boldsymbol{D}_{\text{iso}} = \frac{E_0}{(1+\nu_0)(1-2\nu_0)}\cdot\begin{bmatrix} 1-\nu_0 & \nu_0 & 0 \\ & 1-\nu_0 & 0 \\ SYM & & (1-2\nu_0)/2 \end{bmatrix} \tag{11}$$

$$\boldsymbol{D}_{\text{an}} = \boldsymbol{L}\boldsymbol{D}'\boldsymbol{L}' \quad (\boldsymbol{L}'\text{: transported matrix}) \tag{12}$$

$$\boldsymbol{D}' = \begin{bmatrix} \frac{1-n\nu_2^2}{1-\nu_1}\cdot S & \nu_2 S & 0 \\ & \frac{1-\nu_1}{n}\cdot S & 0 \\ SYM & & G_f \end{bmatrix} \tag{13}$$

in which $S=E_1/(1-\nu_1-2n\nu_2^2)$, $n=E_1/E_2$

$$\boldsymbol{L} = \begin{bmatrix} \cos^2\beta & \sin^2\beta & -2\sin\beta\cos\beta \\ \sin^2\beta & \cos^2\beta & 2\sin\beta\cos\beta \\ \sin\beta\cos\beta & -\sin\beta\cos\beta & \cos^2\beta-\sin\beta^2 \end{bmatrix} \tag{14}$$

In Eq. (13), E_1 and ν_1 are factors relevent to deformation in the direction of the plane of slide or to tensile failure, whereas E_2 and ν_2 are relevant to deformation in a direction normal to the plane (the principal axis of anisotropy).

(4) *Mechanical model for the boundary plane* [6]

We adopted a mechanical model for the boundary plane that took into account displacement restraint and transmission of forces on the boundary plane. We here discuss a model of two materials with different rigidities, for example, in Fig. 7 Mat I (e.g. soil) and Mat II (e.g. concrete) for which the boundary planes are vertical and the normals to the vertical walls are

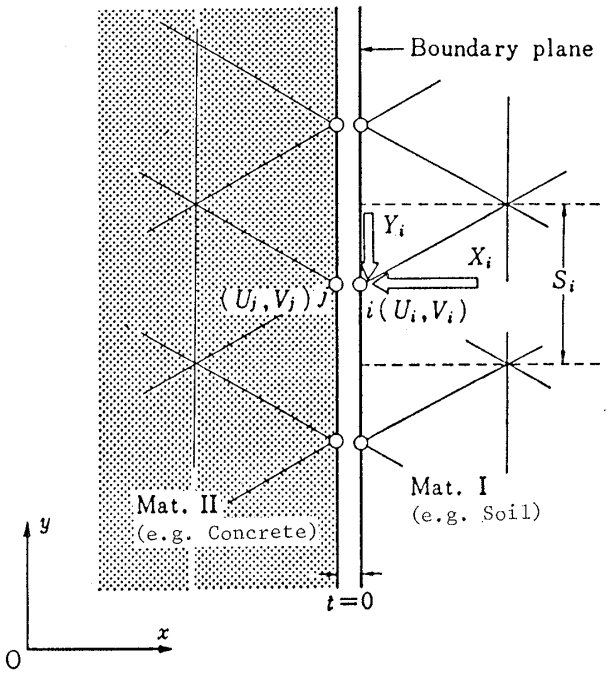

Fig. 7 Mechanical model for the boundary plane.

directed toward the x axis. Attention is paid to the two arbitrary nodal points (i) and (j) on the boundary plane shown in the figure. a nodal point (i) belongs to Mat I, whereas (j) belongs to Mat II, their respective displacements in the x and y directions being (U_i, V_i) and (U_j, V_j).

The nodal forces acting from Mat I to Mat II at nodal point (i) are taken as (X_i, Y_i) and the area of load distribution of nodal point (i) as S_i. Here a sign convention is established so that components of all the nodal forces, displacements, stresses and strains shown in Fig. 8 are positive.

The judgement of slide or separation of nodal points on the boundary plane and the consideration of wall friction (including cohesion along the wall) are illustrated in the flow chart in Fig. 9. F_1, F_2 and F_3 are the safety factors against slide or separation along the wall surface under the corresponding condition, and F_{yi} is the wall friction acting in the y direction on nodal point (i). ϕ' is the effective friction angle of the soil and c' is the soil's cohesion. Condition ($U_i=U_j$, $V_i=V_j$) indicates that the nodes are rigid joints, ($U_i=U_j$, $V_i\neq V_j$) indicates sliding in the y direction and ($U_i\neq U_j$, $V_i\neq V_j$) by separatilon.

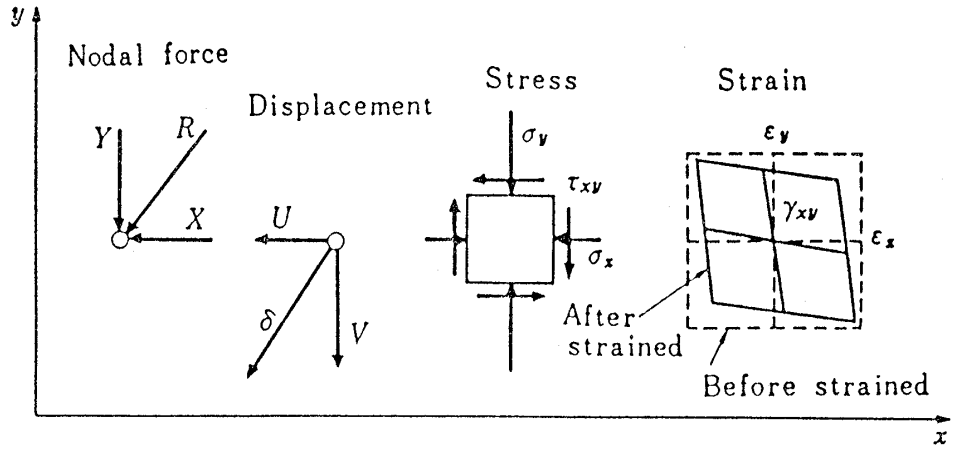

Fig. 8 Positive component: nodal force, displacement, stress and strain.

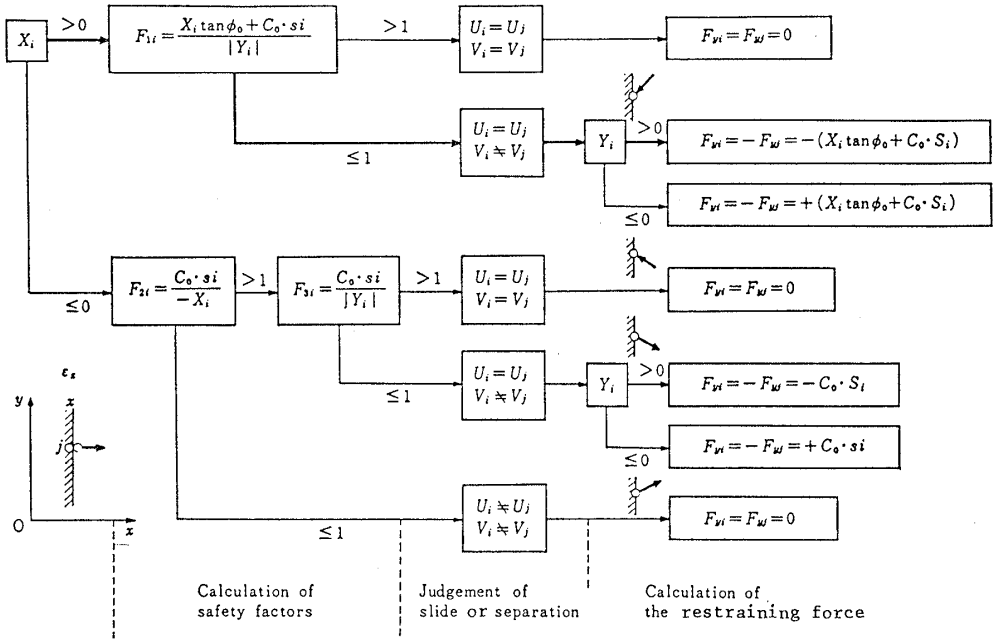

Fig. 9 Flow chart for the calculation of the restraining force.

The analysis procedure is explained by the case shown in the flow chart with the thick line as an example. The compressive force X_i acts on node (j) on the wall surface and because the shear force Y_i is larger than the shearing resistance ($X_i \cdot \tan\phi_0 + c_0 \cdot S_i$) of the wall surface ($F_1 \leqq 1$), the constraint of the nodes (i) and (j), in the y direction is relieved ($V_i \neq V_j$). At the same time, the wall friction, F_{yi} ($=X_i \cdot \tan\phi_0 + c_0 \cdot S_i$), acts on node ($i$) in the upward vertical direction while nodal force, F_{yj}, of same magnitude acts on node (j) in the downward vertical direction as the frictional force imposed by the soil on the wall. Here, ϕ_0 is the angle of wall friction and c_0 is the cohesion between the wall and the soil.

In cases in which the boundary plane is vertical and the normal to the wall is directing the negative direction of x axis, and in which the boundary plane is horizontal, the judgement of sliding or separation, removal of constraints and the consideration of shearing resistance follows a similar procedure.

(5) *Analysis procedure*

We here outline our analysis procedure using Fig. 10. The results of the analysis, i.e., the volumetric water content θ_m and the total head H_m ($m=i, j, k$) of every nodal point at a given time (t) in the seepage flow analysis FEM-A, are the input data for FEM-B. In FEM-B, the degree of saturation of each element $\{S_r\}^e$ is calculated from Eq. (3) and the gravitational force vector $\{W'\}$ for the calculation of effective stress is gained. For example, the weight of an element that

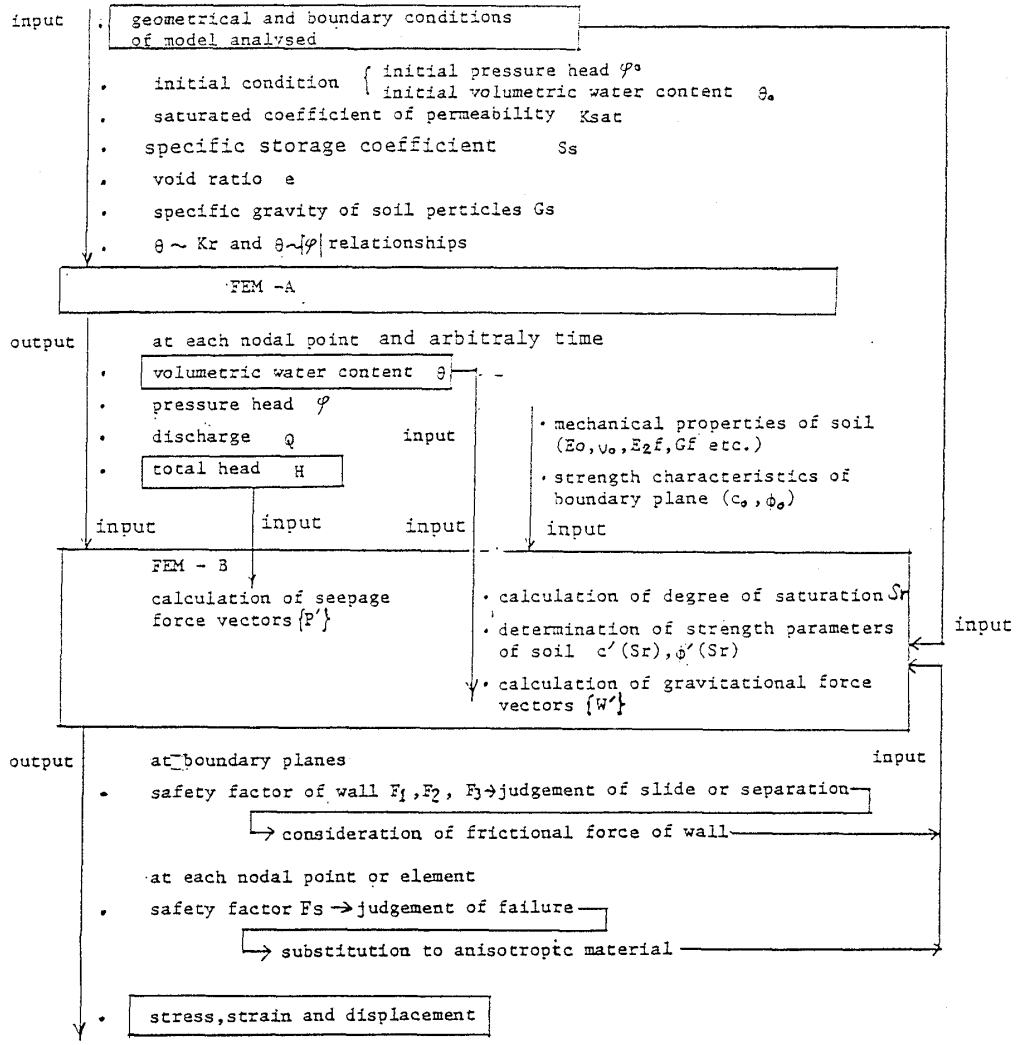

Fig. 10 Flow chart for the method of analysis (FEM-A, B).

lies below the groundwater table is $\gamma' \cdot dvol = \{(G_s - 1) \cdot \gamma_w / (1+e)\} \cdot dvol$. By contrast, the seepage force vector $\{\boldsymbol{P}'\}$ is calculated from H_m in Eq. (8).

(i) First we assume that all the nodes on the boundary surface are so connected as to be perfectly rigid and that the soil layer is an isotropic elastic material, we can obtain the total rigidity matrix $[K]$ from the isotropic stress-strain matrix $\boldsymbol{D}_{iso}$ and the geometrical condition of the model for analysis, because the solutions for the finite elements (stress and nodal forces) being gained because the load vector $\{\boldsymbol{F}\} = \{\boldsymbol{W}'\} + \{\boldsymbol{P}'\}$ is known. (step 1)

(ii) Judgement of the slide and separation of the boundary surface is made from values of F_1, F_2 and F_3 (See Fig. 9) and judgement of the failure of the soil element from the value of F_s in Eq. (9) is made. When the constraint at the nodal points on the boundary surface along which the slide has taken place is released, the shearing-resisting force on the wall is mobilized and the failured element is replaced with anisotropic stress-strain matrix $\boldsymbol{D}_{an}$. In this way, recalculation for the stresses and forces at the nodes is done. (step 2)

(iii) Thereafter, the calculations in (ii) are repeated (steps 3, 4, ···) and when the stage at which no new slide or separation occurs is reached, the solutions are considered to have converged.

4. ANALYTICAL RESULTS OF THE MODEL EXPERIMENT

Determinations of the seepage and stability of the model slope were made by the above method of analysis.

4.1. *FEM-A*

The analytical model for the model slope is shown in Fig. 11. The boundary and initial conditions are given in accordance with the model experiment; *i.e.*, the bottom and side surfaces are considered to be nonpermeable layers.

The first thin layer from the bottom is made of card board that simulates a sand layer, and the 6 layers from the 2nd to 7th tier are filled with the soil. Input is made in accordance with the respective hydraulic properties of the layers. The relation of $\theta \sim |\varphi|$ and $\theta \sim K_r$ of the soil and card board was obtained by testing or other means and shown in Fig. 12. Of the scales on the coordinates axes in the $\theta \sim |\varphi|$ diagram, those marked (1) are for soil and those marked (2) are for card board.

Fig. 13 shows the water table in the soil layer at $t=2$, 15 and 35 min. Fig. 14 is an illustration of the equi-potential lines at $t=35$ min.

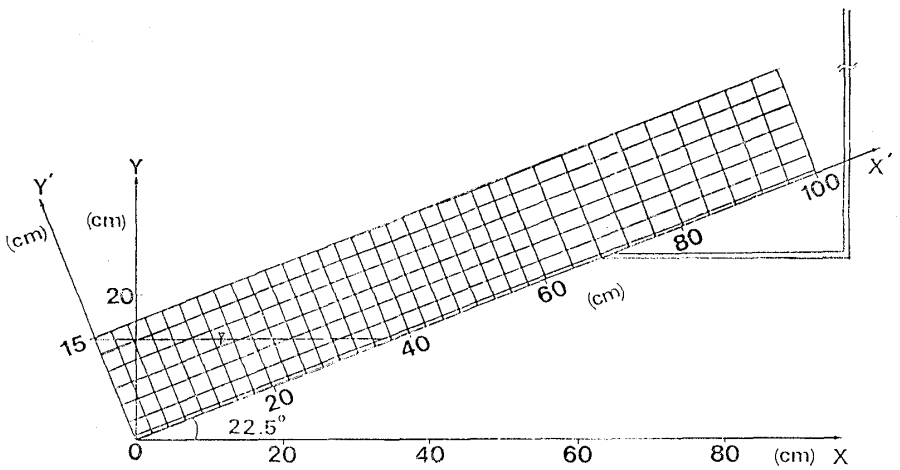

Fig. 11 Analytical model for the model slope.

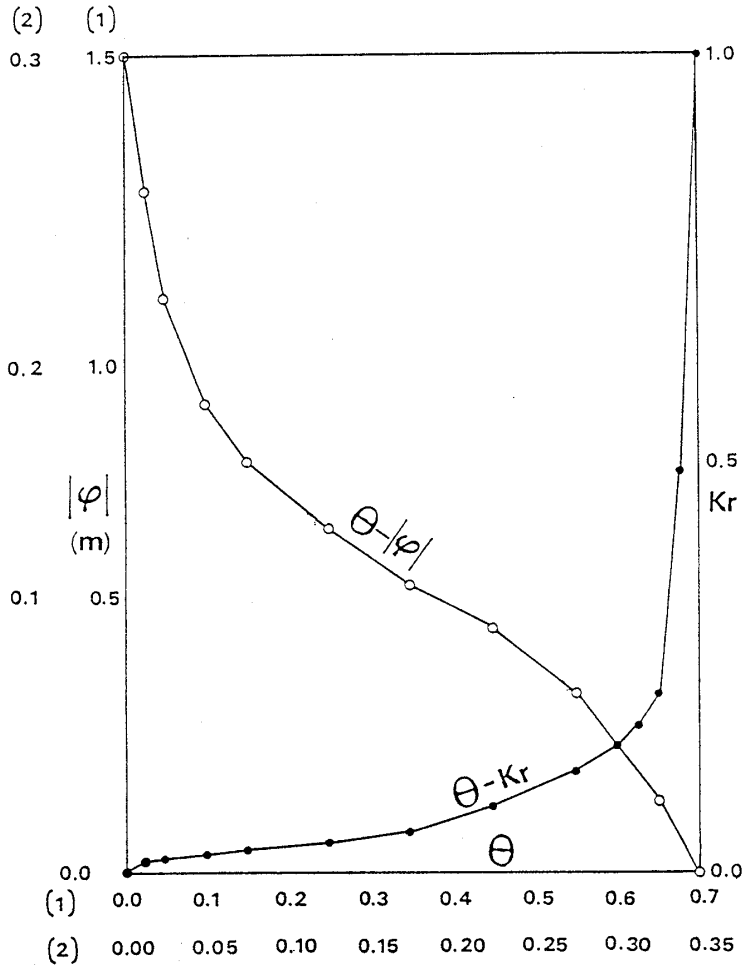

Fig. 12 Relationships between volumetric water content, pressure head and relative conductivity.

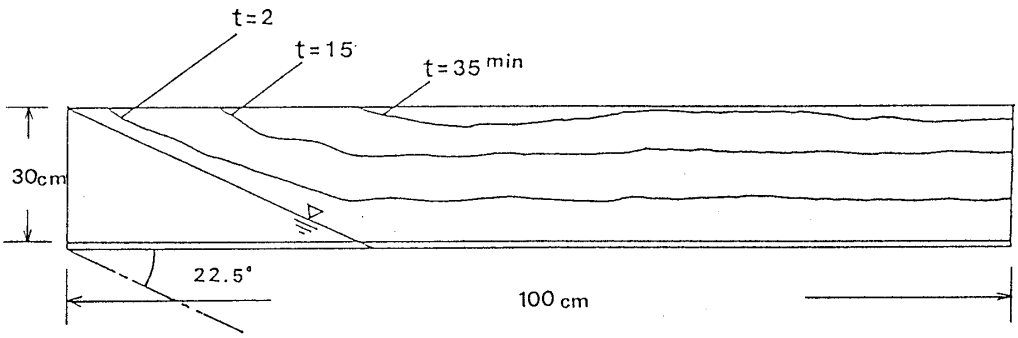

Fig. 13 Variation in the groundwater table in the model slope.

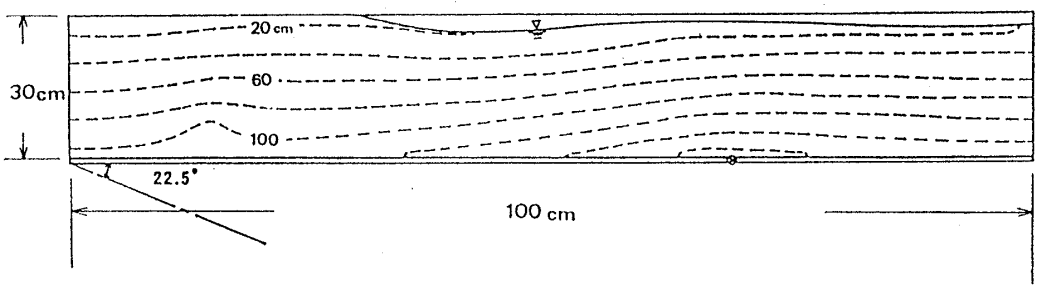

Fig. 14 Equi-potential lines in the model slope (t=35 min).

4.2. *EFM-B*

The rectangular element in Fig. 11 is divided into triangular elements and as the boundaries, the hinged end at the bottom surface of soil layer along the direction of inclination and the roller ends on both sides are used. The coefficients of the deformation of the soil elements before and after failure and the strength parameters at the boundary surface are given in Table 2. Fig. 15 shows the state of failure at $t=2$ min. Fig. 15 (a) shows the safety factor of the elements. The stress conditions of the elements marked with arrows in Fig. 15 (a) are represented by a Mohr's circle (Fig. 15 (b)). Then, Fig. 15 (c) is obtained by decomposing the body force vector into the gravitational force vector $\{W'\}$ and the seepage force vector $\{P'\}$. Fig. 16 shows the condition at $t=35$ min. In Fig. 15 and 16, shading and brack mean tensile failure elements satisfied the condition (II) and (III) in equation (7) respectively. As seen from the diagram, failure

Table 2 Soil parameters used in analysis of the model slope.

Object	Parameter	Symbol	Value
Soil	Unit weight (tf/m³)	γ'	Variable
	Frictional angle (degree)	ϕ'	25.0
	Cohesion (tf/m²)	c'	2.5~25
	Young's modulus at primary (tf/m²)	$E_0=E_1=E_2$	10.0
	Young's modulus at failure (tf/m²)	E_{2f}	0.01
	Shear modulus at primary (tf/m²)	$G_0=E_0/2(1+\nu_0)$	3.85
	Shear modulus at failure (tf/m²)	G_f	0.00385
	Poisson's ratio	ν_0	0.30
Card boad	Young's modulus (tf/m²)	E_c	100.0
	Poisson's ratio	ν_c	0.25

(1 tf/m²=9.8 kPa)

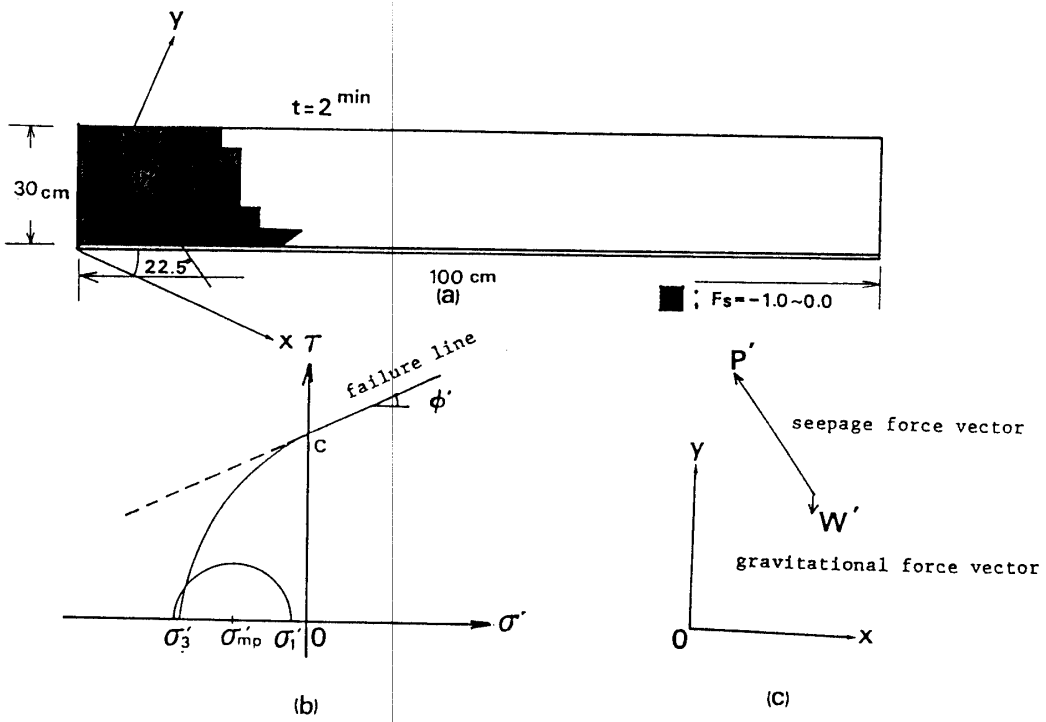

Fig. 15 Development of local failure in the model slope ($t=2$ min).

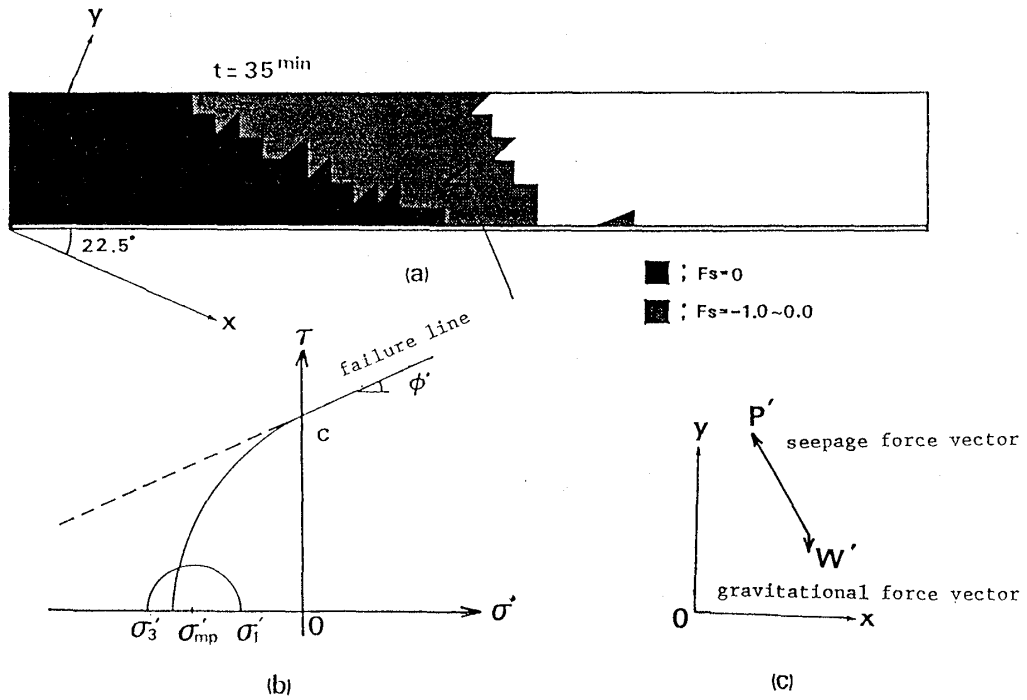

Fig. 16 Development of local failure in the model slope (t=35 min).

starts at the lower end of the model slope. Successively, the slides between the soil layer and the card board initiate at the lower end of the slope and propagate the slope upward.

As time passes, the groundwater table rises and the zone through which it reaches the ground surface expands as shown in Fig. 13. A comparison of Fig. 13 with Figs. 15 and 16 clearly shows that failure proceeds as the zone through which the groundwater table reaches the ground surface expands.

5. SLOPE FAILURE IN THE OKUYAMA AREA

5.1. *Analysis Conditions*

(1) *Rainfall conditions*

The disaster in Nagasaki occurred on July 23, 1982, but there had been considerably heavy rainfall 3 days before. Fig. 17 shows the record of 10-minute's precipitations from July 20th to 23rd, which shows that on July 20th, in particular there was rainfall that continued for 15 hours with 20 mm per hour, followed by an interval of two days with no rainfall. The vast slope failure that occurred was triggered by concentrated rainfall on 23rd. Therefore, as the input of the FEM-A, the amount of precipitation per each 10 minutes on 20th is given for the whole ground surface of the slope. The absence of rain on the 21st and 22nd and the heavy rainfall on the 23rd are given as input. As output, the potential and the degree of saturation are recorded at 30-minute intervals beginning from the first rain on the 20th.

(2) *Analytical model for the Okuyama Slope*

A–A in Fig. 18 was chosen as the longitudinal section to be analyzed based on the topographical map of the Okuyama area prior to the failure. The estimated line of the bed rock determined by a simplified penetration test used in the survey of the slope, and the existence of altered grit was confirmed by the boring tests for the disaster prevention works in the Okuyama area, and its modeling are shown in Fig. 19. From the analytical results described later, a section represented a symbol |↔| in Fig. 19 become clear as the foot of the failure, so this section

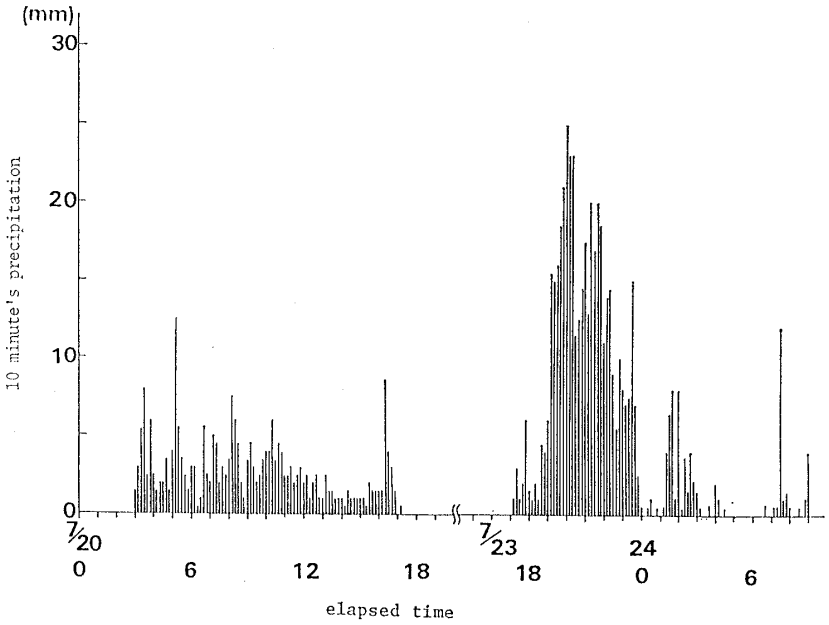

Fig. 17 Rainfall record to July 20–23, 1982 (Nagasaki Marine Meterological Observatory).

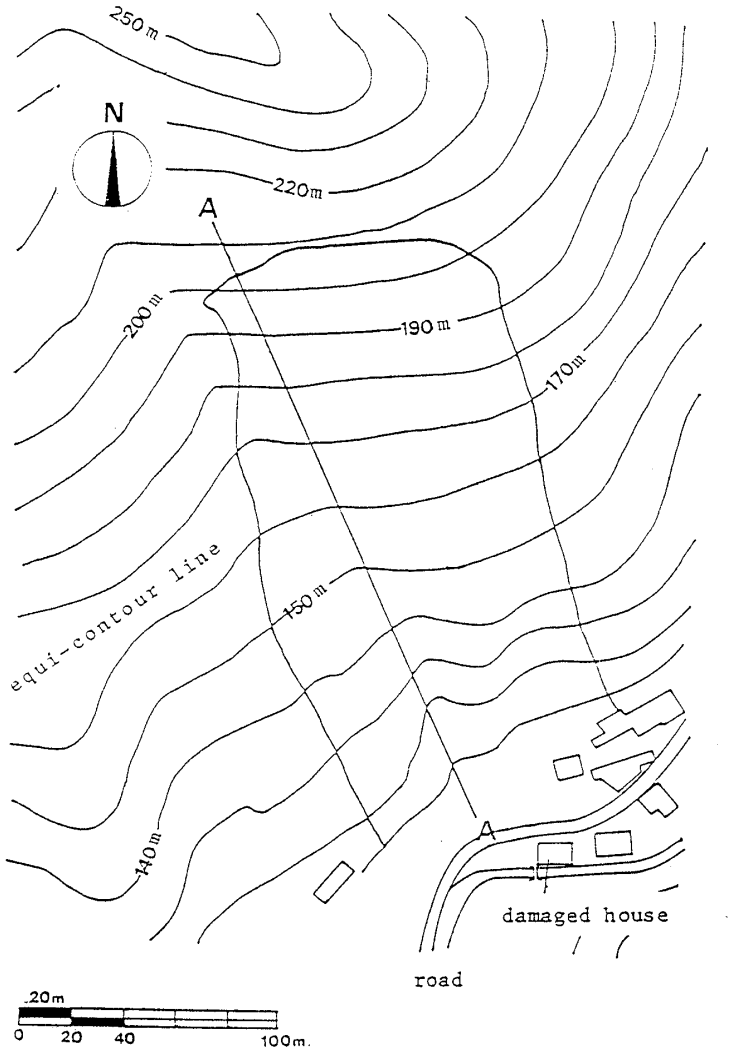

Fig. 18 Topographical map of the Okuyama Area prior to failure.

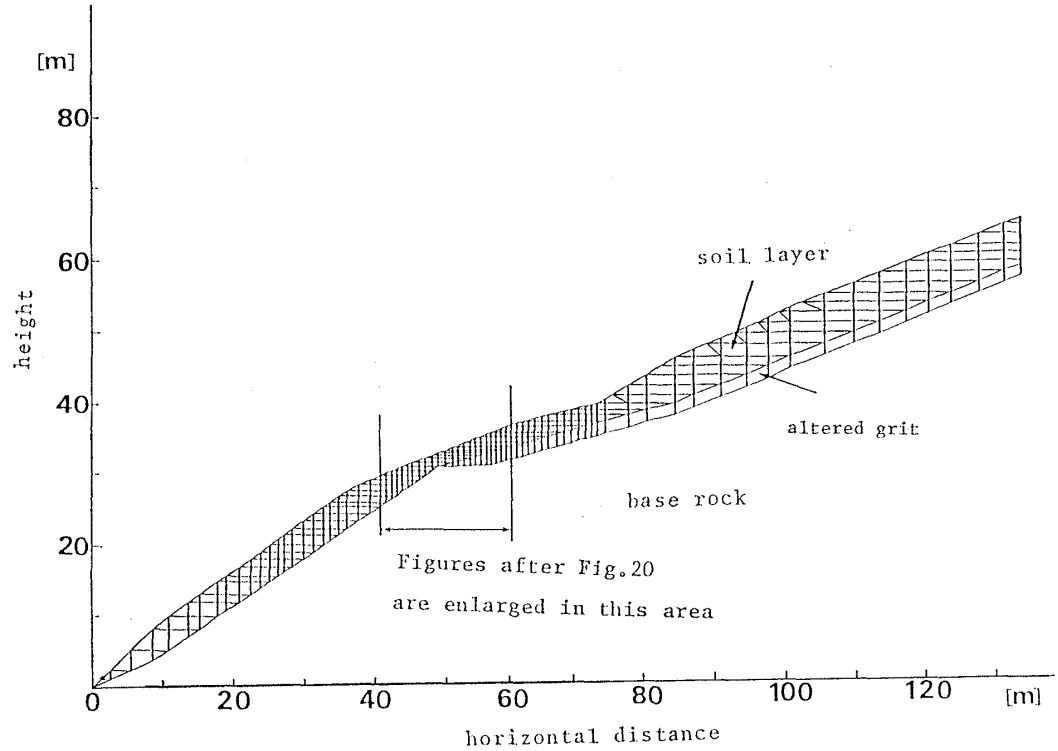

Fig. 19 Analytical model for the Okuyama Slope.

are enlarged in the figures after Fig. 20.

(3) *Soil properties*

The properties of soil layer are given in Table 3. These properties were determined by the block-sampling method and the method of sand replacement on the spot, and the coefficient of permeability and the density of the altered grit were estimated. Judging the saturated permeability of soil layer, most of all the precipitation on the 23rd should be discharged as a surface flow.

(4) *Others*

The relations of $\theta \sim |\varphi|$, $\theta \sim K_r$ in Fig. 12 were adopted, it was assumed that the lower end of the slope lay above the surface of seepage and that the 2-dimensional vertical problem could be analyzed by backward difference.

The initial conditions of FEM-B and the physical properties of the material used are given

Table 3 Soil properties of the Okuyama Slope.

Object	Parameter	Symbol	Value
Soil	Liquid limit (%)	W_L	71.9
	Plastic limit (%)	W_P	37.8
	Natural water content (%)	W_n	38.6
	Void ratio	e	1.39
	Unit weight at primary (tf/m^3)	γ'	1.585
	Coefficient of permeability (cm/s)	K_{sat}	1.95×10^{-4}
	Degree of saturation at primary (%)	S_r	76.0
	Japanese unified classification		MH
Card boad	Coefficient of permiability (cm/s)	K_{sat}	1.0×10^{-1}

Table 4 Soil parameters used in the analysis of the Okuyama Slope.

Object	Parameter	Symbol	Value
Soil	Unit weight (tf/m³)	γ'	Variable
	Frictional angle (degree)	ϕ'	25.0
	Cohesion (tf/m²)	c'	7.5~75
	Young's modulus at primary (tf/m²)	$E_0=E_1=E_2$	100.0
	Young's modulus at failure (tf/m²)	E_{2f}	0.1
	Shear modulus at primary (tf/m²)	$G_0=E_0/2(1+\nu_0)$	38.5
	Shear modulus at failure (tf/m²)	G_f	0.0385
	Poisson's ratio	ν_0	0.30
Alterd grit	Young's modulus (tf/m²)	E_g	1000.0
	Poisson's ratio	ν_g	0.25
Boundary	Frictional angle (degree)	ϕ_0	15.43
	Cohesion (tf/m²)	c_0	Variable

(1 tf/m²=9.8 kPa)

in Table 4.

5.2. *Analytical Results under Actual Conditions*

Because the actual conditions at the time of the failure must be reproduced from the beginning of the rainfall on the 20th, the analysis was made by giving the input of the rainfall conditions starting at 03:00 on the 20th and at 30-minute intervals thereafter under the conditions described below.

The groundwater table rose due to the rainfall on the 20th, but fell during the two rainless days that followed, then it rose again due to the heavy rainfall on the 23rd. The groundwater table at 18:00 and 18:30 are shown in Fig. 20 in order to compare the time of slope failure there-

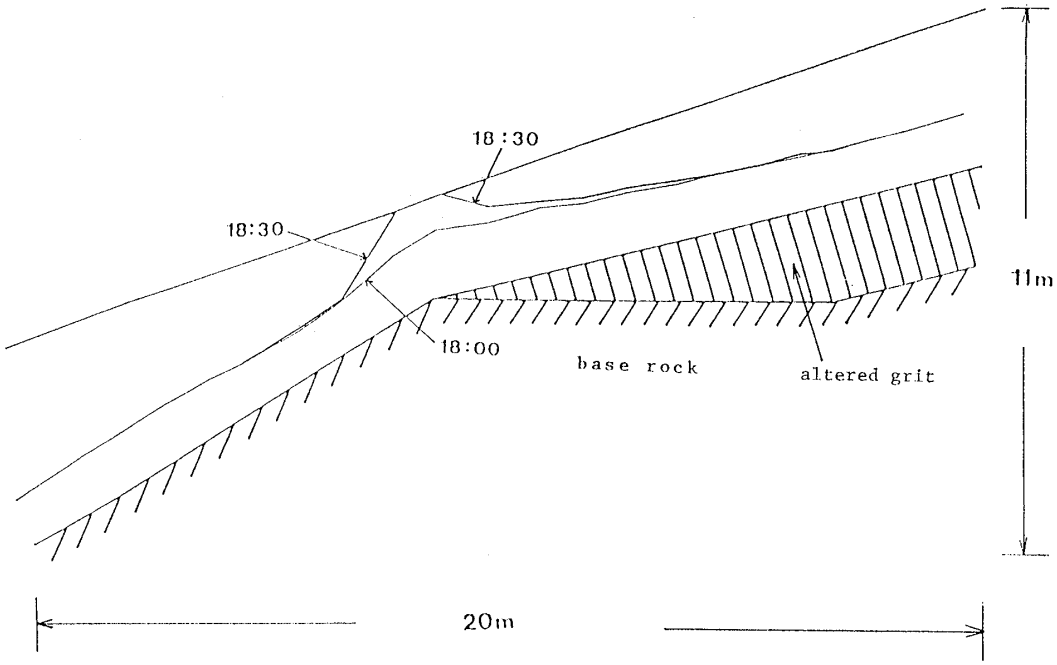

Fig. 20 Variation in the groundwater table in the Okuyama Slope (Actual Case: 23rd).

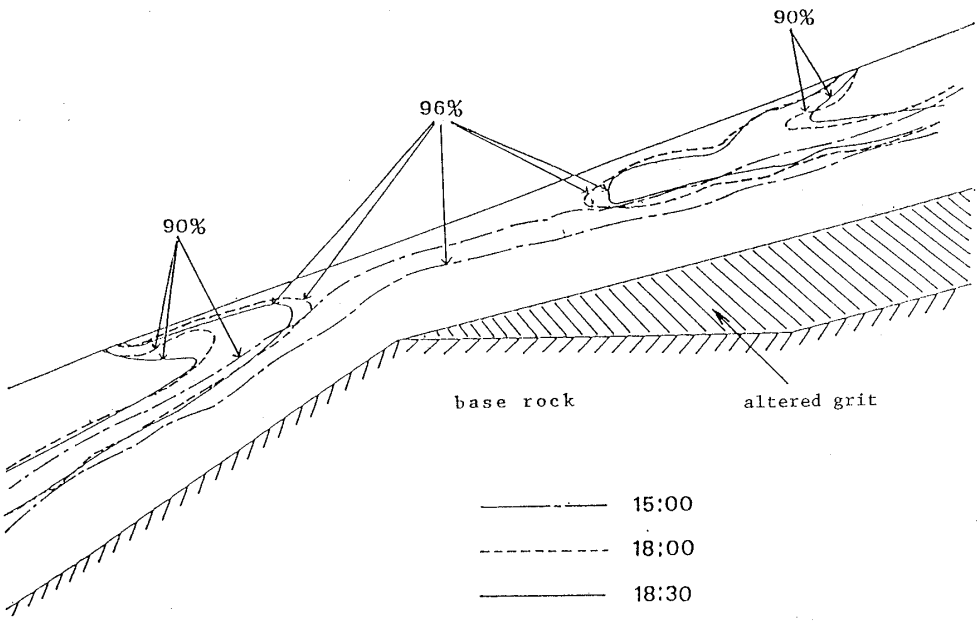

Fig. 21 Distribution of the degree of saturation in the Okuyama Slope (Actual Case: 23rd).

after. At 18:00 the middle portion of the groundwater table bulges slightly upward, and at 18:30 the table interescts the ground surface.

The degree of saturation changed due to the rainfall on the 23rd and remained fairly high when rainfall started. By 18:00, it is elevated to the heights and at 18:30 has developed to the conditions shown in Fig. 21.

The method used in the model analysis described previously was used to determine the stability of the slope. The stability at 18:00 is shown in Fig. 22 (a) and that at 18:30 in Fig. 22 (b). The notation $Fs=0\sim1.0$ and $Fs=1.0\sim0$ indicate the zone of shear and tensile failure respectively. As seen from the diagram, at 18:00 the local failure reaches the ground surface, and slides between the soil layer and the altered grit simultaneously intiate at this area, and propagate the slope upward gradually. So, slope failure is believed to start from this area.

5.3. *Analytical Results under Different Conditions*

To determine the causes of failure at the site of the disaster, as well as to consider possible occurrences in other fresh and gentle slopes, we must investigate failure under condition that differ from the actual ones. Although numerous combinations of factors could have been considered, the existence of the preceding rainfall (on the 20th) and the altered grit were chosen as the variable factors. Case A in which there is no preceding rainfall but altered grit exists; Case B in which there is preceding rainfall but no altered grit, and Case C in which there is neither preceding rainfall nor altered grit were investigated.

(1) *Case A*

The groundwater table shown in Fig. 23 is lower than that under actual conditions shown in Fig. 20. Fig. 24 is the distribution diagram of the degree of saturation. Because the rise in the degree of saturation of the soil layers started from the initial value $S_r=76\%$, it is logical that the rise in the degree of saturation is lower than that reported in Fig. 21. With respect to stability, the failure zone does not reach the ground surface as shown in Fig. 25 (a) and (b); but, later at 20:30, conditions of failure similar to those shown in Fig. 22 (a) and (b) are reached and failure takes place.

(2) *Case B*

As shown in Fig. 26, by 18:30 the groundwater table has risen similar to the actual case

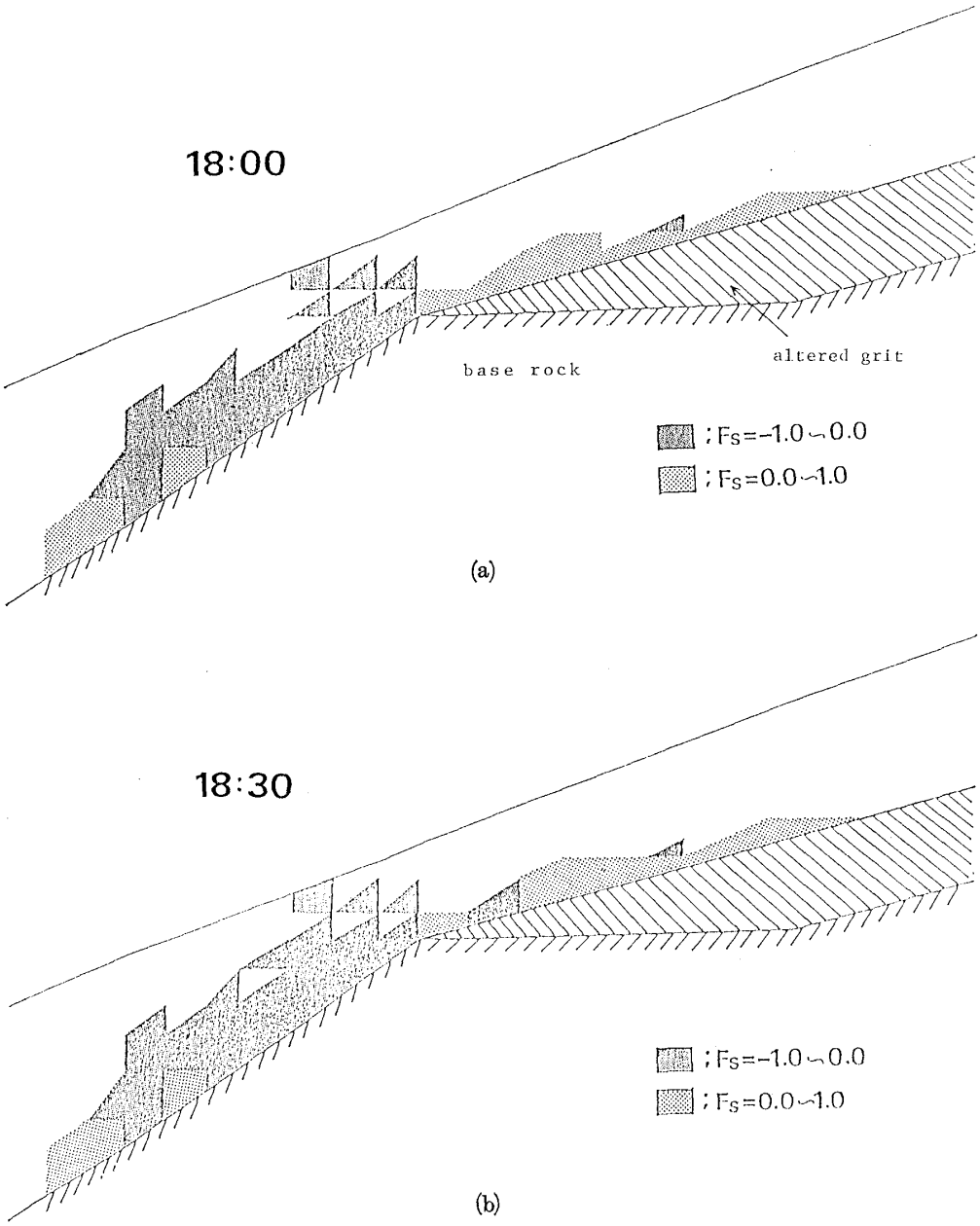

Fig. 22 Development of local failure in the Okuyama Slope (Actual Case: 23rd): (a) 18:00; (b) 18:30.

(Fig. 21). Distinctive features of the distribution of the degree of saturation in Fig. 27 are the rises along the bed rock from below simular to Fig. 21. The degree of saturation has risen in most parts by 18:00 and by 18:30.

In our analysis of the actual conditions, we compared Figs. 20, 21 and 22 with Figs. 26, 27 and 28, and found that when the groundwater table rises and the area in which intersects the ground surface widens, the slope failure leading to a gigantic land-slide could take place. So, we concluded that the preceding rainfall (on the 20th) significantly influenced on the slope failure in comparison with the existence of the altered grit. If the position of the groundwater table is determined in advance as criterion for the stability of the slope, it would be possible to forecast the slope failure by recording the rise of the groundwater table.

Fig. 28 (a) shows that the generation of failure is limited to the soil layer beneath the ground

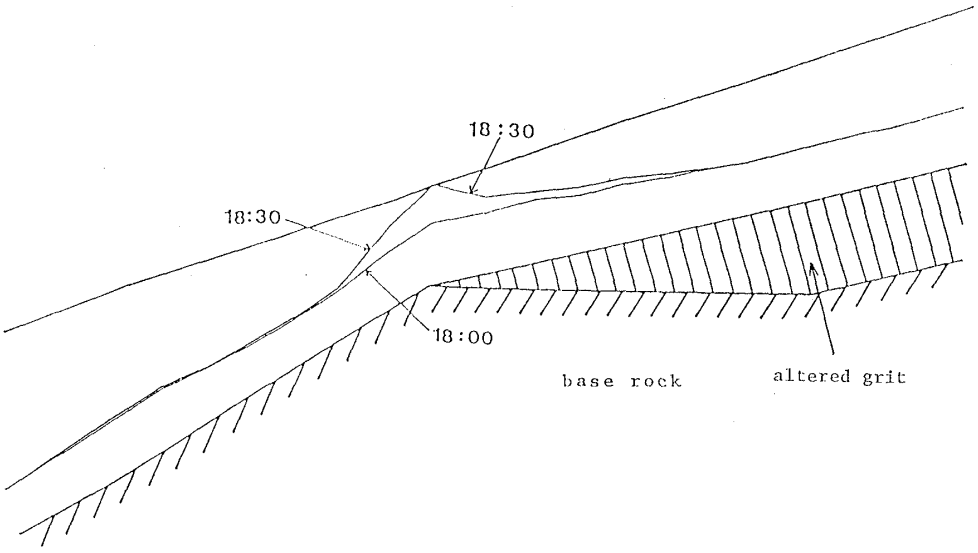

Fig. 23 Variation in the groundwater table in the Okuyama Slope (case A).

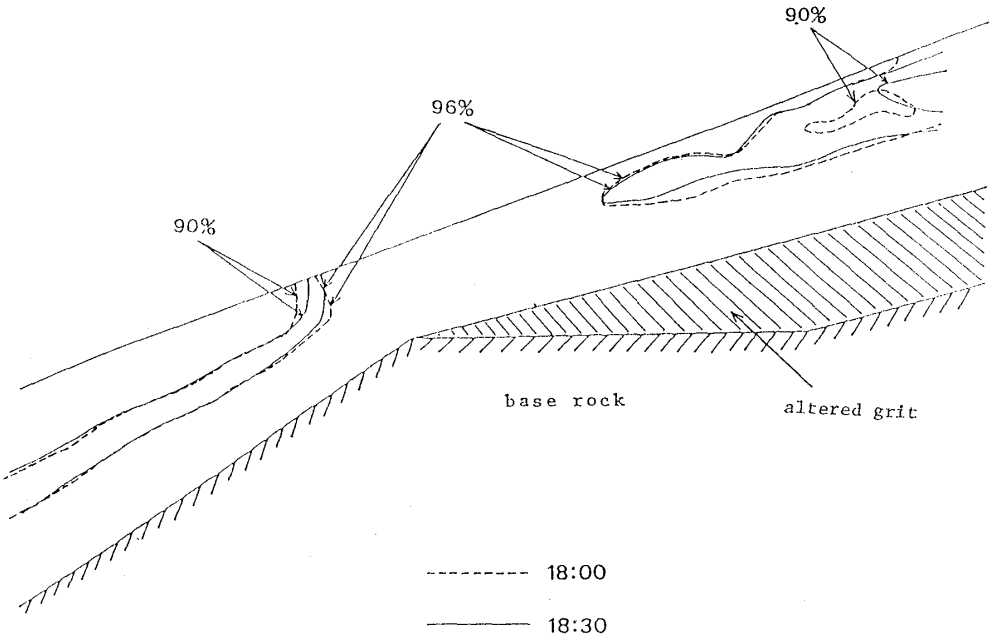

Fig. 24 Distribution of the degree of saturation in the Okuyama Slope (case A).

surface at 18:00, but by 18:30, failure has reached the ground surface (Fig. 28 (b)).

(3) *Case C*

Diagrams for the groundwater table, distribution of the degree of saturation and local failure are omitted because they are similar to those for case B with no preceding rainfall.

Because of the existence of the thin soil layer at the slight bend of the bed rock in the middle of the slope, the groundwater table rises locally (Figs. 20, 23 and 26), and the area over which the groundwater table reaches the ground surface widens, after which failure occurs (Figs. 22 and 28). In contrast, if the area over which the groundwater table reaches the ground surface is very small, there is no failure (Fig. 25). These true observations also hold for Figs. 13, 15 and 16 which show the results of our analysis of the model experiment. The analytical results are summarized in Table 5. The exact time of slope failure in the Okuyama area is not known,

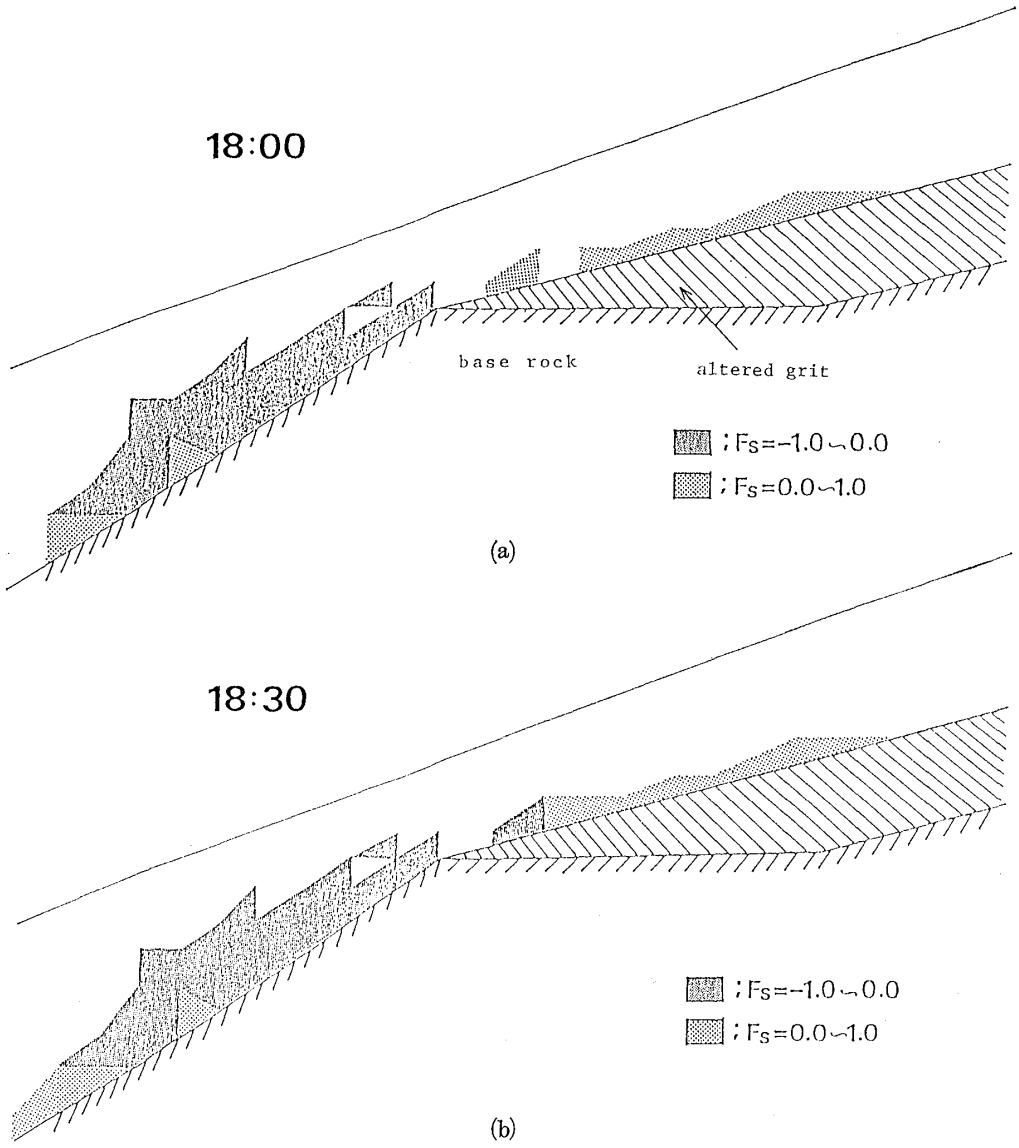

Fig. 25 Development of local failure in the Okuyama Slope (case A): (a) 18:00; (b) 18:30.

Table 5 Conditions and results of FEM analysis of the Okuyama Slope.

Cases	Preceding Rain	Altered Grit	Free Surface of ground water	Failure	Fig. to be referred
Actual condition	Yes	Yes	Remarkable rise, an area over which it intersects with the ground surface generates and spread	Occurred at 18:00	Fig. 20, 21, 22
Case A	No	Yes	Just contacts the ground surface	No. but occurred at 20:30	Fig. 23, 24, 25
Case B	Yes	No	Remarkable rise, an area over which it intersects with the ground surface generates and spread	Occurred at 18:30	Fig. 26, 27, 28
Case C	No	No	Just contacts the ground surface	No, but occurred at 20:30	None

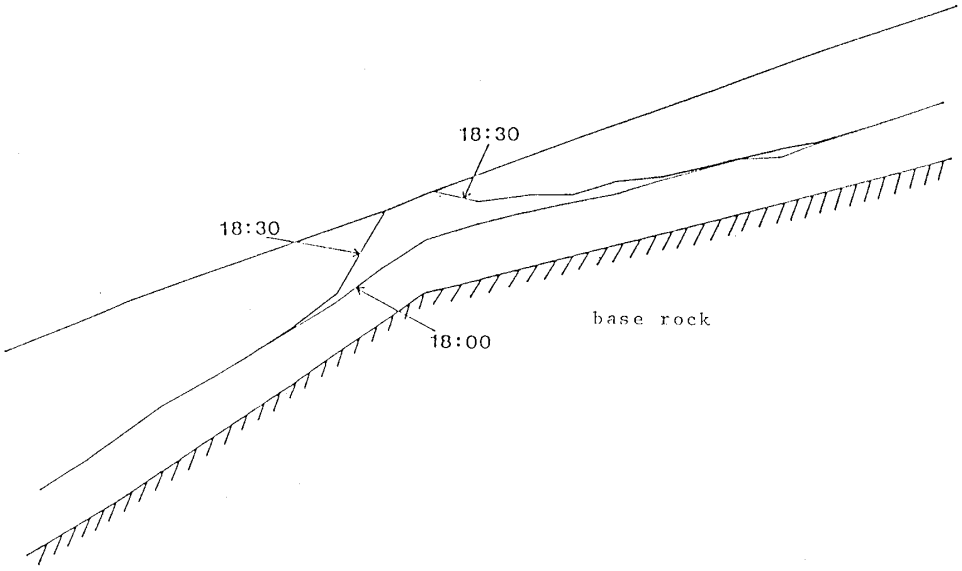

Fig. 26 Variation in the groundwater table in the Okuyama Slope (case B).

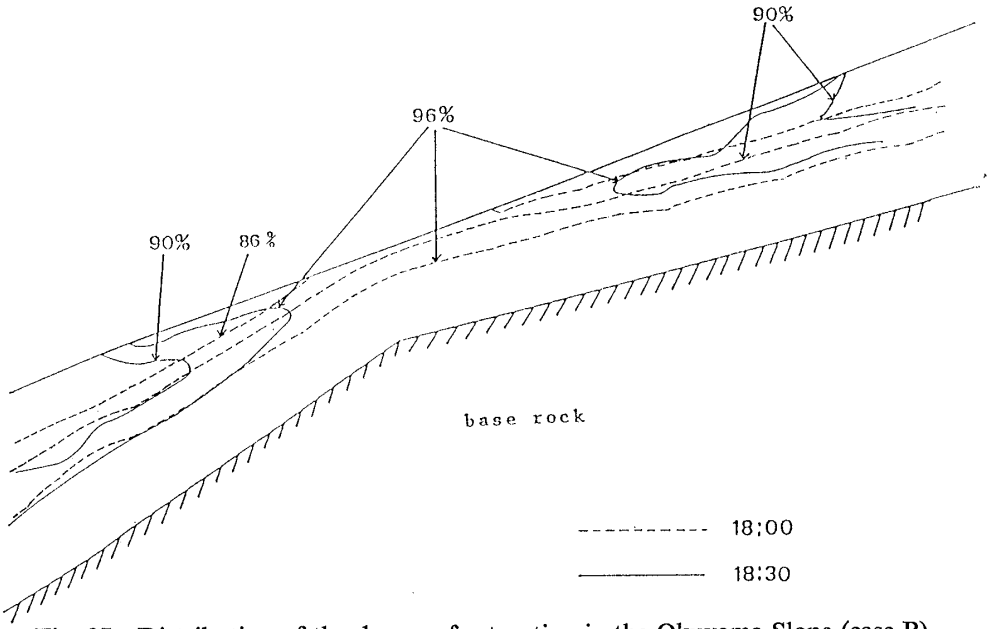

Fig. 27 Distribution of the degree of saturation in the Okuyama Slope (case B).

but by the neighbors's speaking, it might be occurred at 20:15 around. For this case also, if the position of the groundwater table and the expansion of it to the point at which failure might occur are determined in advance with respect to the stability of the slope, our accuracy in forecasting slope failure would be improved by simple observations of these phenomena. This table clearly shows that the factor of preceding rainfall strongly effects the occurrence of slope failure, whereas the existence of altered grit has little effect.

5.4. *Conclusions*

To investigate the failure generated along a gentle slope at the time of heavy rainfall, we chose to analyze a gigantic landslide occurred in the Okuyama area of Nagasaki city on July 23, 1982, and we conclude that

(1) Even a gentle slope with angle of inclination of 22.5° could collapse if the seepage force

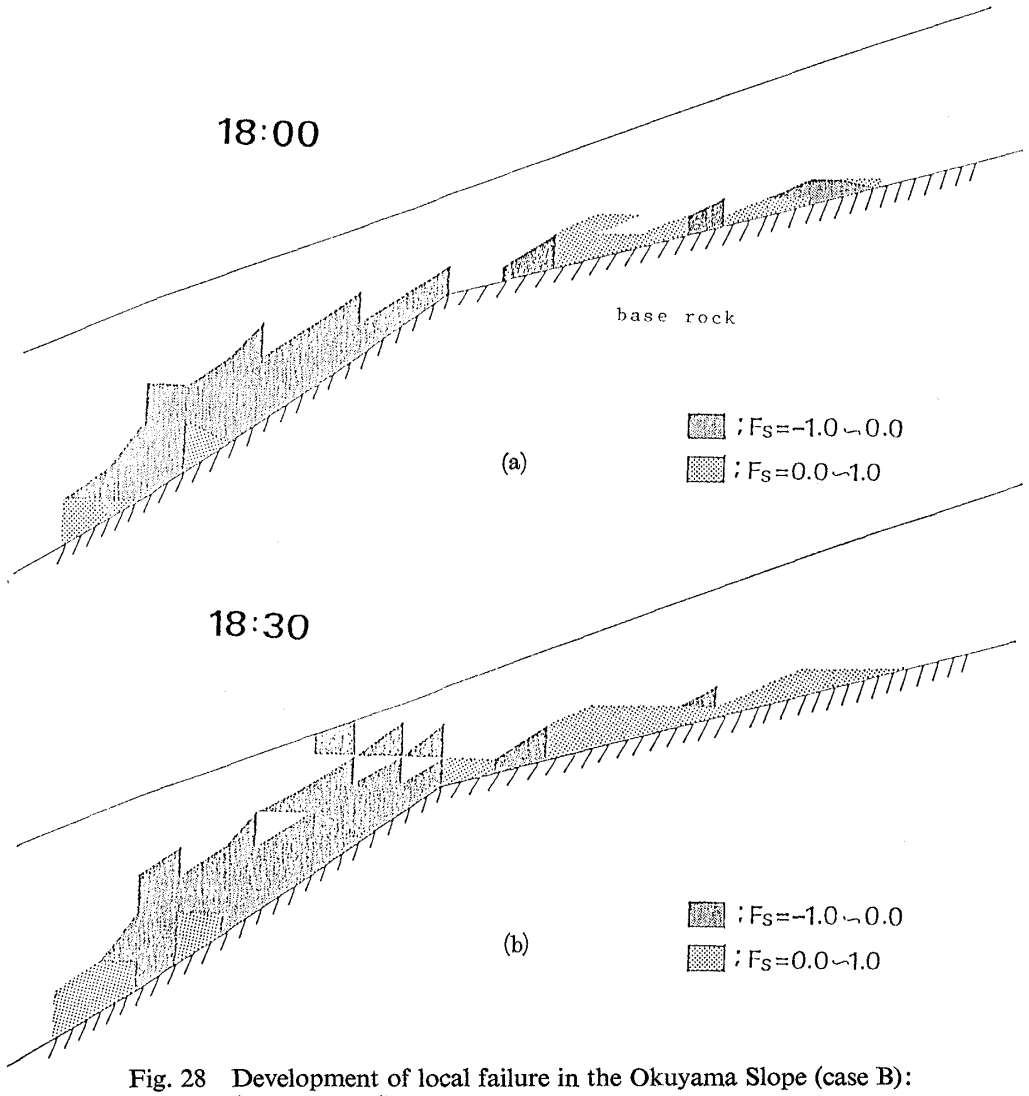

Fig. 28 Development of local failure in the Okuyama Slope (case B): (a) 18:00; (b) 18:30.

is taken into account.

(2) The preceding rainfall (on the 20th) significantly influences on the slope failure.

(3) The geomorphology of the site shows a layer of altered grit, but this layer had little effect on the generation of failure.

(4) With regard to the stability of slope, if the position of the groundwater table at which failure occurs can be determined in advance, our accuracy in forecasting slope failure will improve by recording the rise in the level of the groundwater table.

6. SLOPE FAILURE IN THE HOKUEI-CHO AREA [8]

Our analysis of the Okuyama slope failure showed that the seepage force participates in triggering slope failure due to permeation of rain water. The Okuyama slope had, however, a number of variables such as altered grit and changes in the gradients of the slope and bed rock. We therefore chose a slope structure which has a relatively simple geomorphology, a failured slope in the Hokuei-cho area of Nagasaki City and analyzed its mechanism of failure.

6.1. *Analysis Conditions*

Fortunately, the geological survey and soil exploration of the area in which this slope is located have been completed. The longitudinal or profile section to be analyzed is located at the center of the map shown in Fig. 29. The longitudinal section is given in Fig. 30 which shows that the bed rock layer has a linear gradient and that the thickness of the top soil layer ranges from 2~4 m, which makes this profile with small changes. The gradient of the slope is 35° and is steeper than that of the Okuyama slope, making the degree of slope safety much lower. The values of the soil properties, its strength and coefficients of the deformation are shown in Tables 6 and 7.

6.2. *Analytical Results under Actual Conditions*

The influence of preceding rainfall on the Okuyama slope failure being significant, the rainfall from July 20th also was considered in this analysis. The groundwater table was at the posi-

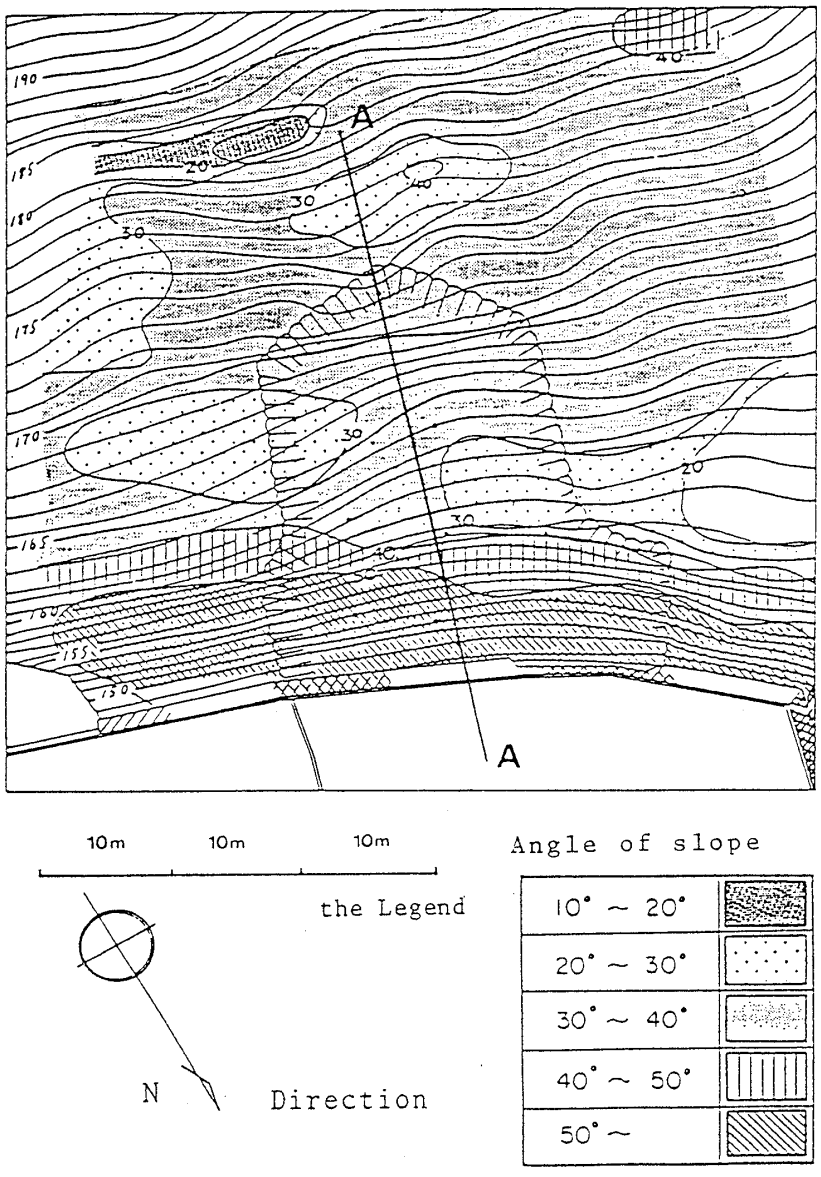

(After the Reference (1))

Fig. 29 Topographical map of the Hokuei-cho Slope after failure.

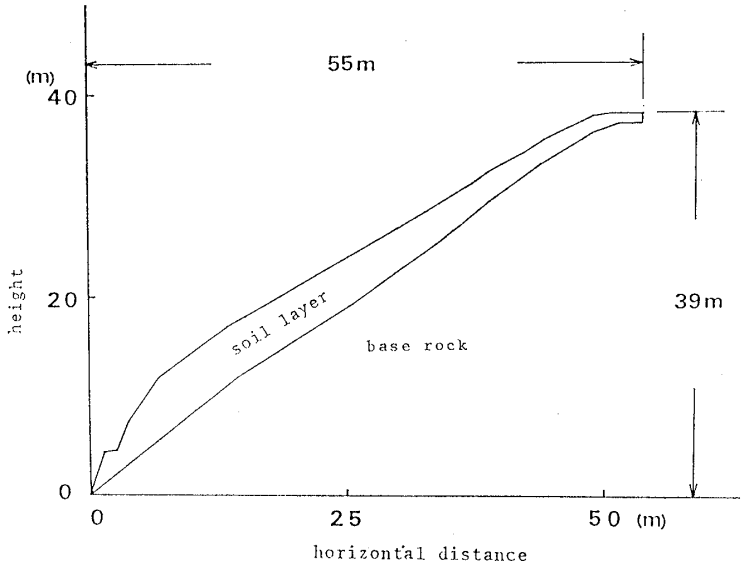

Fig. 30 Analytical model for the Hokuei-cho Slope.

Table 6 Soil properties of the Hokuei-cho Slope.

Object	Parameter	Symbol	Value
Soil	Liquid limit (%)	W_L	48.3
	Plastic limit (%)	W_P	30.5
	Natural water content (%)	W_n	34.6
	Void Ratio	e	1.36
	Unit weight at primary (tf/m³)	γ'	1.53
	Coefficient of permeability (cm/s)	K_{sat}	3.75×10^{-5}
	Degree of Saturation at primary (%)	S_r	61.0
	Japanese unified classification		ML

Table 7 Soil parameters used in the analysis of the Hokuei-cho Slope.

Object	Parameter	Symbol	Value
Soil	Unit weight (tf/m³)	γ'	Variable
	Frictional angle (degree)	ϕ'	20.0
	Cohesion (tf/m²)	c'	8.0~12
	Young's modulus at primary (tf/m²)	$E_0=E_1=E_2$	1000.0
	Young's modulus at failure (tf/m²)	E_f	1.0
	Shear modulus at primary (tf/m²)	$G_0=E_0/2(1+\nu_0)$	357.0
	Shear modulus at failure (tf/m²)	G_f	0.357
	Poisson's ratio	ν_0	0.40
Boundary	Frictional angle (degree)	ϕ_0	13.6
	Cohesion (tf/m²)	c_0	0.533

(1 tf/m²=9.8 kPa)

tion shown in Fig. 31 (a) at 17:00 July 23rd, just before the heavy rainfall on that day, and by 18:00 the groundwater had reached the slope surface due to the heavy rainfall, and by 23:00 the area of seepage has expanded further (Fig. 31 (b)). The distribution of the degree of satura-

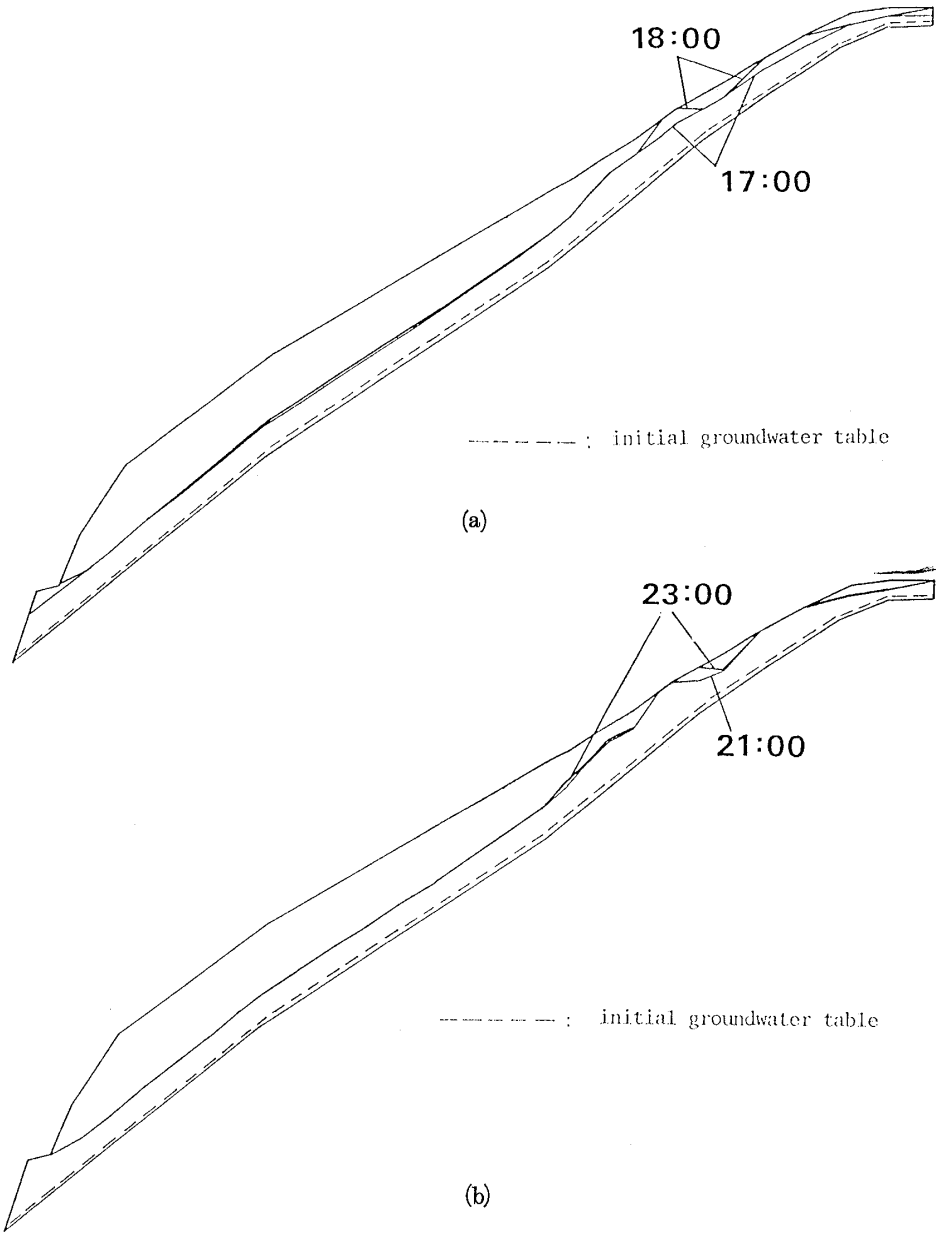

Fig. 31 Variation in the groundwater table in the Hokuei-cho Slope (Actual Case: 23rd): (a) 17:00 and 18:00; (b) 21:00 and 23:00.

tion at 17:00 on 23rd is shown in Fig. 32 (a) and at 18:00 in Fig. 32 (b). In these diagrams, the rise in the original degree of saturation to the preceding rainfall already is recognizable at 17:00.

Fig. 33 (a), (b) and (c) show the respective stabilities of the soil elements at 17:00, 18:00 and 23:00 on July 23, evidence that tensile failure was generated in elements close to the ground surface.

6.3. *Analytical Results under Different Conditions*

As the steepness of the gradient of the Hokuei-cho slope reaches 35°, we used FEM-B analysis to determine the mechanism of failure, disregarding the seepage force, and considering only the action of the gravitational forces. The results show that there is no element in which tensile failure takes place. The diagrams of stability obtained resemble the one obtained by omitting the elements of F_s=—1.0~0 (Fig. 34).

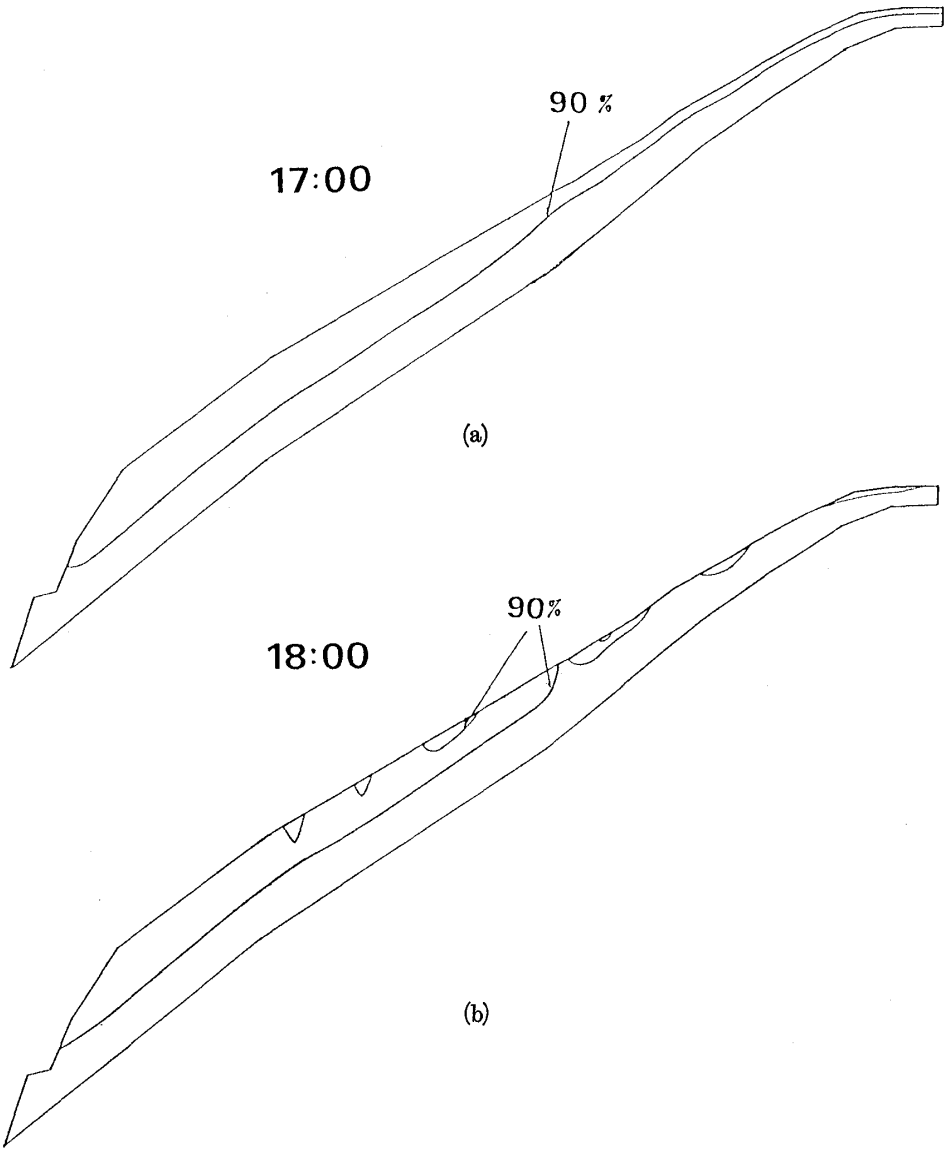

Fig. 32 Distribution of the degree of saturation in the Hokuei-cho Slope (Actual Case: 23rd): (a) 17:00; (b) 18:00.

6.4. *Conclusions*

From FEM-B analysis of the Hokuei-cho slope, we concluded that

(1) Although the gradient of the slope is fairly steep at 35°, no generation of tensile failure in the soil layer would be made by the action of gravity force, but when the seepage force also is working the slope collapses due to the generation of tensile failure.

(2) The tensile failure zone generated in the soil layer produced by the seepage force widen as the groundwater table rises.

(3) Because the gradient of the slope is linear and its geological structure is simple, any rise of the groundwater table would be conspicuous at locations where the soil layer is thin. This is because the actual flow velocity of the permeation of rain water with a natural water content (measured in a laboratory test) is about 5 times the velocity at the saturated condition and because of locations where the soil layer is thin. Therefore, there is the faster rise of the groundwater table because rain water that permeates from the ground surface reaches bed rock sooner.

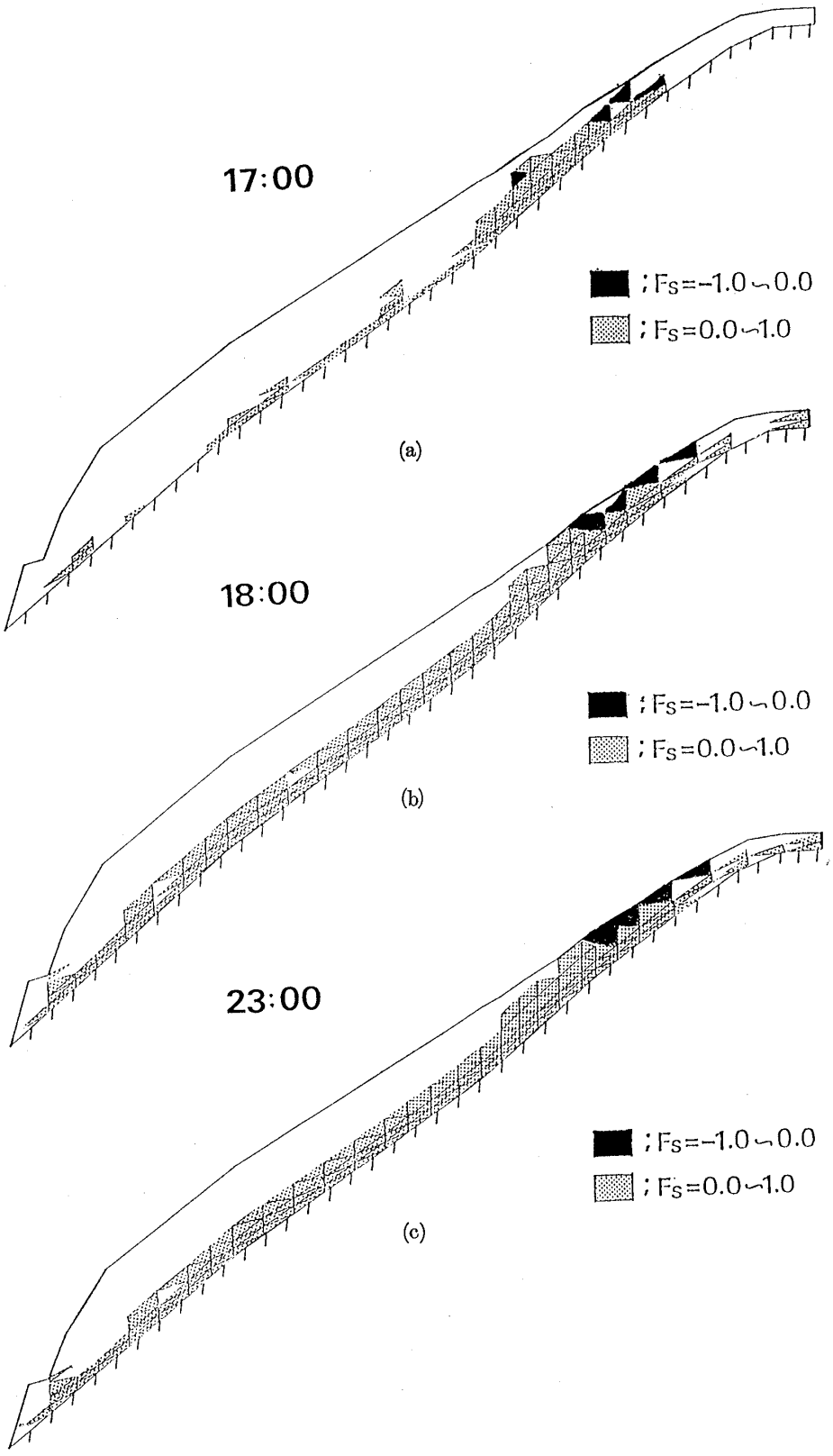

Fig. 33 Development of local failure in the Hokuei-cho Slope (Actual Case: 23rd): (a) 17:00; (b) 18:00; (c) 23:00.

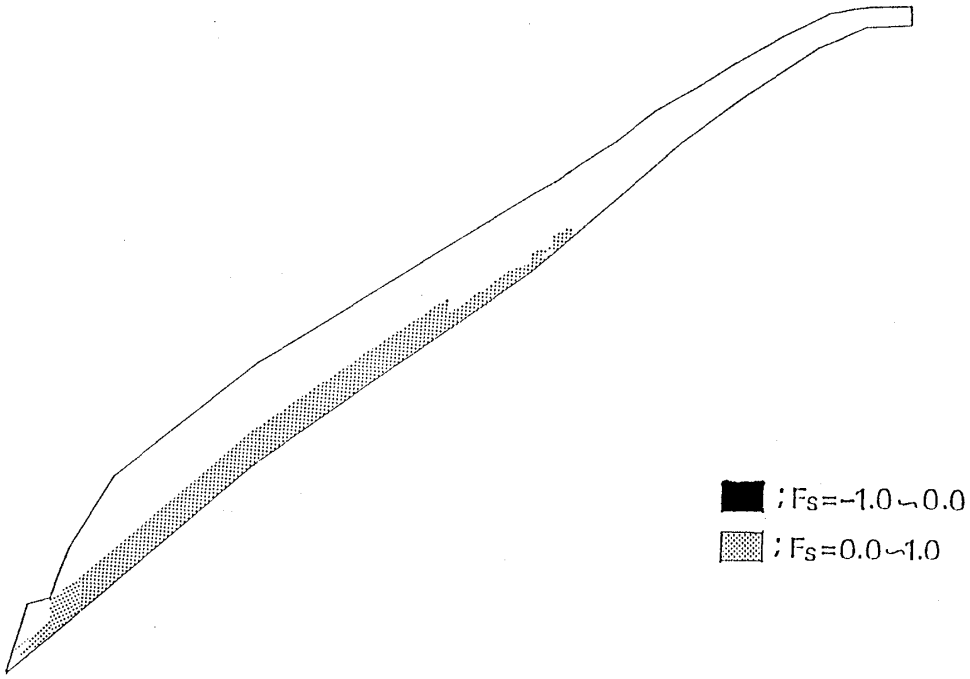

Fig. 34 Development of local failure in the Hokuei-cho Slope (seepage force not taken into account).

7. SUMMARY

To determine the mechanism of slope failure at the time of the July 23, 1982 ,the heavy rainfall in Nagasaki, we used saturated-unsaturated seepage flow analysis to study slopes in the Okuyama and Hokuei-cho areas. We also used stability analysis to study the slopes taking into account the seepage force and the reduction of strength due to the rise of the degree of saturation.

The analytical results of the gentle Okuyama slope (angle of inclination is 22.5°) show that even on a gentle slope, failure can occur due to the effect of the seepage force and that preceding rainfall accelerates slope failure. Results also show that the slope in Hokuei-cho area (mean gradient is 35°) did not reach the point of failure due to only the gravity force; clearly, the preceding rainfall and seepage force participated in the slope failure.

We have shown that slope failure can be forecast if a rise in the groundwater table can be detected. Development of this technique is greatly needed to upgrade our forecasting technology in order to prevent disasters caused by slope failures.

ACKNOWLEDGEMENT

This study was subsidized by Special Research Funds for Natural Disasters from the Ministry of Education Culture and Science of Japan.

REFERENCES

[1] Science and Technology Agency of Japan (1985). Emergency Technical Report on the Nagasaki Heavy Rainfall Disaster, July 1982, pp. 115–137 (in Japanese).

[2] Nagasaki University Scientific Investigation Team (1982). Report on the Investigation of the Nagasaki Heavy Rainfall Desaster, July 1982, pp. 59–71 (in Japanese).

[3] Iseda, T., Tanabashi, Y. and Yamamoto, Y. (1985). A study of gentle slope failure at the Nagasaki Heavy Rainfall, JSMFE, Vol. 25, No. 2, pp. 173–184 (in Japanese).

[4] Akai, K., Onishi, Y. and Nishigaki, M. (1979). Finite element analysis of saturated-unsaturated seepage in soil, JSCE, Vol. 264, pp. 87–96 (in Japanese).
[5] Kudara, K. (1983). A Study of the Collapse of Embankments and Countermeasures, Dr. of Eng., Dissertation, Kyushu University, pp. 26–33 (in Japanese).
[6] Iseda, T., Tanabashi, Y. and Higuchi, T. (1979). Finite element analysis taking into account wall friction, the 14th Japan National Conference on Soil Mechanics and Foundation Engineering, pp. 989–992 (in Japanese).
[7] Hasegawa, H. and Ikeuchi, M. (1964). On the tensile strength test of disturbed soils, Rheology and Soil Mech., IUTAM Symp, Grenoble, pp. 405–412.
[8] Yamamoto, Y., Iseda, T., Tanabashi, Y., Nagamatsu, M., Mine, Y. and Baba, M. (1985). Finite element analysis of slope failure taking into account seepage flow, JSCE Regional Conference, Western Branch, pp. 342–343 (in Japanese).